

1

Synthesis, Characterization, and Selected Properties of Graphene

C. N. R. Rao, Urmimala Maitra, and H. S. S. Ramakrishna Matte

1.1 Introduction

Carbon nanotubes (CNTs) and graphene are two of the most studied materials today. Two-dimensional graphene has specially attracted a lot of attention because of its unique electrical properties such as very high carrier mobility [1–4], the quantum Hall effect at room temperature [2, 5], and ambipolar electric field effect along with ballistic conduction of charge carriers [1]. Some other properties of graphene that are equally interesting include its unexpectedly high absorption of white light [6], high elasticity [7], unusual magnetic properties [8, 9], high surface area [10], gas adsorption [11], and charge-transfer interactions with molecules [12, 13]. We discuss some of these aspects in this chapter. While graphene normally refers to a single layer of sp^2 bonded carbon atoms, there are important investigations on bi- and few-layered graphenes (FGs) as well. In the very first experimental study on graphene by Novoselov *et al.* [1, 2] in 2004, graphene was prepared by micromechanical cleavage from graphite flakes. Since then, there has been much progress in the synthesis of graphene and a number of methods have been devised to prepare high-quality single-layer graphenes (SLGs) and FGs, some of which are described in this chapter.

Characterization of graphene forms an important part of graphene research and involves measurements based on various microscopic and spectroscopic techniques. Characterization involves determination of the number of layers and the purity of sample in terms of absence or presence of defects. Optical contrast of graphene layers on different substrates is the most simple and effective method for the identification of the number of layers. This method is based on the contrast arising from the interference of the reflected light beams at the air-to-graphene, graphene-to-dielectric, and (in the case of thin dielectric films) dielectric-to-substrate interfaces [14]. SLG, bilayer-, and multiple-layer graphenes (<10 layers) on Si substrate with a 285 nm SiO_2 are differentiated using contrast spectra, generated from the reflection light of a white-light source (Figure 1.1a) [15]. A total color difference (TCD) method, based on a combination of the reflection spectrum calculation and the International Commission on Illumination (CIE) color space

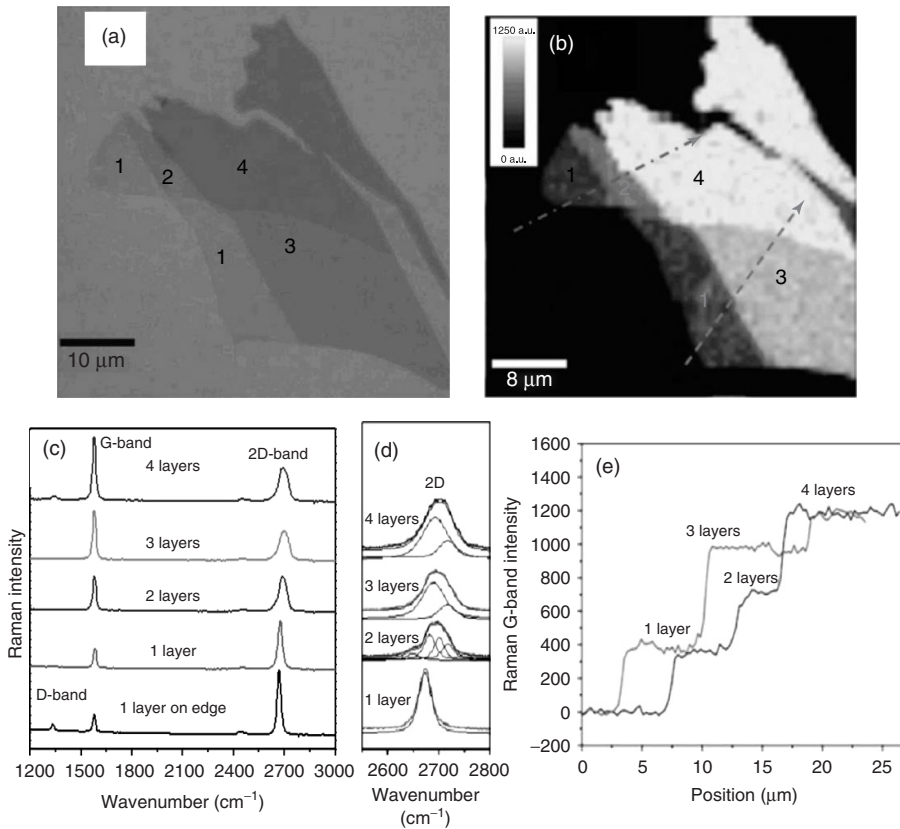


Figure 1.1 (a) Optical image of graphene with one, two, three, and four layers; (b) Raman image plotted by the intensity of G-band; (c) Raman spectra as a function of the number of layers; (d) zoom-in view

of the Raman 2D-band; and (e) the cross section of the Raman image, which corresponds to the dashed lines in (b). (Source: Reprinted with permission from Ref. [15].)

is also used to quantitatively investigate the effect of light source and substrate on the optical imaging of graphene for determining the thickness of the flakes. It is found that 72 nm thick Al₂O₃ film is much better at characterizing graphene than SiO₂ and Si₃N₄ films [16].

Contrast in scanning electron microscopic (SEM) images is another way to determine the number of layers. The secondary electron intensity from the sample operating at low electron acceleration voltage has a linear relationship with the number of graphene layers (Figure 1.2a) [17]. A quantitative estimation of the layer thicknesses is obtained using attenuated secondary electrons emitted from the substrate with an in-column low-energy electron detector [18]. Transmission electron microscopy (TEM) can be directly used to observe the number of layers on viewing the edges of the sample, each layers corresponding to a dark line. Gass *et al.* [19] observed individual atoms in graphene by high-angle annular

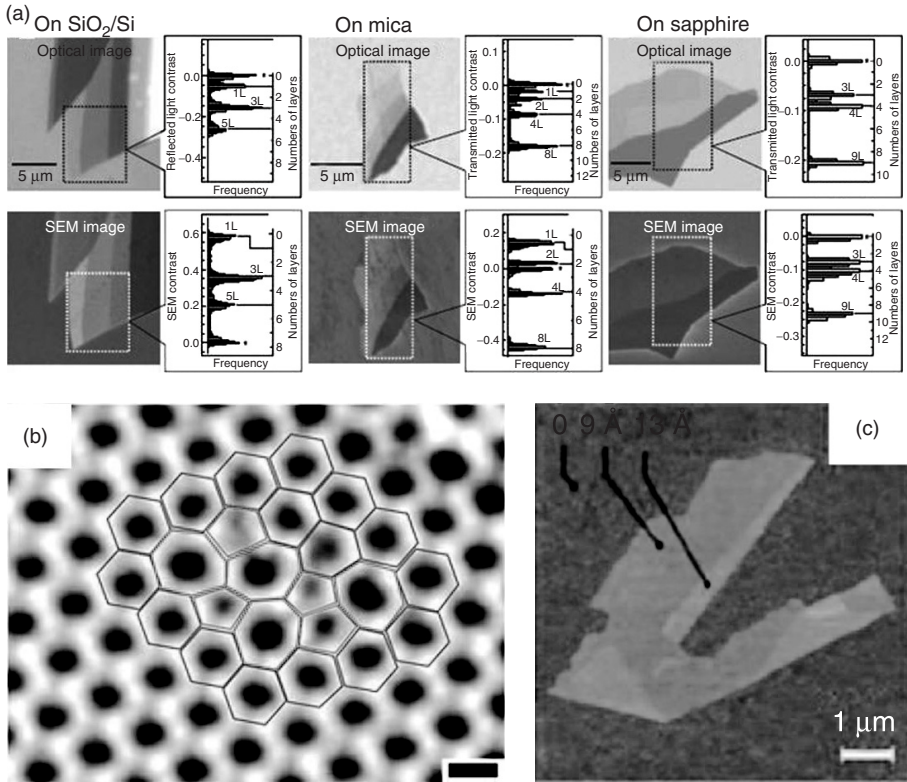


Figure 1.2 (a) Comparison of the counting of layers by optical microscopy and SEM for graphene on SiO₂/Si, mica, and sapphire. For each figure is shown a histogram of the distribution of graphene layers within the rectangular area indicated by a dotted line. (Source: Reprinted with permission from Ref. [17].) (b) High-resolution

transmission electron microscopic image showing the Stone–Wales defects in graphene. (Source: Reprinted with permission from Ref. [20].) (c) Atomic force microscopic image of single-layered graphene. Folded edge shows a height increase of 4 Å indicating single-layer graphene. (Source: Reprinted with permission from Ref. [3].)

dark-field (HAADF) scanning transmission electron microscopy (STEM) in the aberration-corrected mode at an operation voltage of 100 kV. Direct visualization of defects in the graphene lattice, such as the Stone–Wales defect, has been possible by aberration-corrected TEM with monochromator (Figure 1.2b) [20]. Electron diffraction can be used for differentiating the single layer from multiple layers of graphene. In SLG, there is only the zero-order Laue zone in the reciprocal space, and the intensities of diffraction peaks do not therefore, change much with the incidence angle. In contrast, bilayer graphene exhibits changes in total intensity with different incidence angles. Thus, the weak monotonic variation in diffraction intensities with tilt angle is a reliable way to identify monolayer graphene [21]. The relative intensities of the electron diffraction pattern from the {2110} and {1100} planes can be used to determine the number of layers. If $I_{\{1100\}}/I_{\{2110\}}$ is

>1 , it is reported as SLG, and if the ratio is <1 , it is multilayer graphene [22]. Thickness of graphene layers can be directly probed by atomic force microscopy (AFM) in tapping mode. On the basis of the interlayer distance in graphite of 3.5 \AA [3], the thickness of a graphene flake or the number of layers is determined as shown in Figure 1.2c [3]. Scanning tunneling microscopy (STM) also provides high-resolution images of graphene.

Raman spectroscopy has been extensively used as a nondestructive tool to probe the structural and electronic characteristics of graphene [3]. Figure 1.1c shows typical Raman spectra of one-, two-, three-, and four-layered graphene prepared using micromechanical cleavage technique and placed on SiO_2/Si substrate. The Raman spectrum of graphene has three major bands. The D-band located around 1300 cm^{-1} is a defect-induced band. The G-band located around 1580 cm^{-1} is due to in-plane vibrations of the sp^2 carbon atoms. The 2D-band around 2700 cm^{-1} results from a second-order process. The appearance of the D- and 2D-bands is related to the double resonance Raman scattering process [23], and with the increasing the number of layers, the 2D-band gets broadened and blue shifted. A sharp and symmetric 2D-band is found in the case of SLG as shown in Figure 1.1d. The Raman image obtained from the intensity of the G-band is shown in Figure 1.1b. A linear increase in the intensity profile of the G-band with increase in the number of layers along the dashed line is shown in Figure 1.1e [15]. Surface area, which also forms an important characteristic of graphene, is discussed later in the chapter.

1.2

Synthesis of Single-Layer and Few-Layered Graphenes

SLG and FG have been synthesized by several methods. In Table 1.1, we have listed some of these methods. The synthesis procedure can be broadly classified into exfoliation, chemical vapor deposition (CVD), arc discharge, and reduction of graphene oxide.

Table 1.1 Synthesis of single- and few-layered graphene.

Graphene synthesis	
Single layer	Few layers
Micromechanical cleavage of HOPG	Chemical reduction of exfoliated graphene oxide (2–6 layers)
CVD on metal surfaces	
Epitaxial growth on an insulator (SiC)	Thermal exfoliation of graphite oxide (2–7 layers)
Intercalation of graphite	Aerosol pyrolysis (2–40 layers)
Dispersion of graphite in water, NMP	
Reduction of single-layer graphene oxide	Arc discharge in presence of H_2 (2–4 layers)

1.2.1

Mechanical Exfoliation

Stacking of sheets in graphite is the result of overlap of partially filled p_z or π orbital perpendicular to the plane of the sheet (involving van der Waals forces). Exfoliation is the reverse of stacking; owing to the weak bonding and large lattice spacing in the perpendicular direction compared to the small lattice spacing and stronger bonding in the hexagonal lattice plane, it has been tempting to generate graphene sheets through exfoliation of graphite (EG). Graphene sheets of different thickness can indeed be obtained through mechanical exfoliation or by peeling off layers from graphitic materials such as highly ordered pyrolytic graphite (HOPG), single-crystal graphite, or natural graphite. Peeling and manipulation of graphene sheets have been achieved through AFM and STM tips [24–29]. Greater control over folding and unfolding could be achieved by modulating the distance or bias voltage between the tip and the sample [29]. Zhang [30] obtained 10–100 nm thick graphene sheets using graphite island attached to tip of micromachined Si cantilever to scan over SiO_2/Si surface. Folding and tearing of the sheets arise due to the formation of sp^3 -like line defects in the sp^2 graphitic network, occurring preferentially along the symmetry axes of graphite.

Novoselov *et al.* [1] pressed patterned HOPG square meshes on a photo resist spun over a glass substrate followed by repeated peeling using scotch tape and then released the flakes so obtained in acetone. Some flakes got deposited on the SiO_2/Si wafer when dipped in the acetone dispersion. Using this method, atomically thin graphene sheets were obtained. This method was simplified to just peeling off of one or a few sheets of graphene using scotch tape and depositing them on SiO_2 (300 nm)/Si substrates. Although mechanical exfoliation produces graphene of the highest quality (with least defects), the method is limited due to low productivity. Chemical exfoliation, on the other hand, possesses the advantages of bulk-scale production.

1.2.2

Chemical Exfoliation

Chemical exfoliation is a two-step process. The first step is to increase the interlayer spacing, thereby reducing the interlayer van der Waals forces. This is achieved by intercalating graphene to prepare graphene-intercalated compounds (GICs) [21]. The GICs are then exfoliated into graphene with single to few layers by rapid heating or sonication. A classic example of chemical exfoliation is the generation of single-layer graphene oxide (SGO) prepared from graphite oxide by ultrasonication [31–36]. Graphene oxide (GO) is readily prepared by the Hummers method involving the oxidation of graphite with strong oxidizing agents such as KMnO_4 and NaNO_3 in $\text{H}_2\text{SO}_4/\text{H}_3\text{PO}_4$ [31, 33]. On oxidation, the interlayer spacing increases from 3.7 to 9.5 Å, and exfoliation resulting in SLG is achieved by simple ultrasonication in a DMF/water (9 : 1) (dimethyl formamide) mixture. The SGO so prepared has a high density of functional groups, and reduction needs to be carried

out to obtain graphene-like properties. Chemical reduction has been achieved with hydrazine monohydrate to give well-dispersed SLG sheets [32, 35]. Thermal exfoliation and reduction of graphite oxide also produce good-quality graphene, generally referred to as reduced graphene oxide (RGO).

Rapid heating ($>200^\circ\text{C min}^{-1}$) to 1050°C also breaks up functionalized GO into individual sheets through evolution of CO_2 [37, 38]. A statistical analysis by AFM has shown that 80% of the observed flakes are single sheets [38]. Exfoliation of commercial expandable graphite has also been carried out by heating at 1000°C in forming gas for 60 s [39]. The resultant exfoliated graphite was reintercalated with oleum and tetrabutylammonium hydroxide (TBA). On sonication in a DMF solution of 1,2-distearoyl-*sn*-glycero-3-phosphoethanolamine-*N*-[methoxy-(polyethylene glycol)-5000] (DSPE-mPEG) for 60 min, the graphite-containing oleum and TBA get exfoliated to give a homogeneous suspension of SLG. These sheets can be made into large, transparent, conducting assembly in a layer-by-layer manner in organic solvents. On rapid heating, decomposition rate of the epoxy and hydroxyl groups of GO exceeds the diffusion rate of the evolved gases resulting in pressures that exceed the van der Waals forces holding the graphene sheets together and then exfoliation occurs. Exfoliated graphene sheets are highly wrinkled and have defects. As a result, these sheets do not collapse back to graphite but remain as highly agglomerated graphene sheets. Guoqing *et al.* [40] used microwaves to give thermal shock to acid-intercalated graphite oxide in order to carry out exfoliation. When irradiated in microwave oven, eddy currents are generated because of the stratified structure of GO, yielding high temperatures by Joule's heating. Decomposition and gasification of the intercalated acids in graphite leads to a sudden increase in interlayer spacing and thereby reduces van der Waals interaction. Further sonication yields SLG and FG sheets. Liang *et al.* [41] patterned FG on SiO_2/Si substrates using the electrostatic force of attraction between HOPG and the Si substrate. Laser exfoliation of HOPG has also been used to prepare FG, using a pulsed neodymium-doped yttrium aluminum garnet (Nd:YAG) laser [42]. The product depends on laser fluence, a fluence of $\sim 5.0 \text{ J cm}^{-2}$, yielding high-quality graphene with ultrathin morphology.

GICs can be prepared by the intercalation of alkali metal ions. Viculis *et al.* [43] prepared K-, Cs-, and NaK_2 -intercalated graphite by reacting alkali metals with acid-intercalated exfoliated graphite in Pyrex sealed tubes. GICs were treated with ethanol causing a vigorous reaction to yield exfoliated FG. A schematic representation of the reaction is presented in Figure 1.3a. Potassium-intercalated GICs are also prepared using the ternary potassium salt $\text{K}(\text{THF})_x\text{C}_{24}$, and they get readily exfoliated in *N*-methylpyrrolidone (NMP), yielding a dispersion of negatively charged SLG that can then be deposited onto any substrate [44].

Solution-phase EG in an organic solvent such as NMP results in high SLG yields [22]. In this case, the energy required to exfoliate graphene is balanced by the solvent-graphene interaction. Such solvent-graphene interactions are

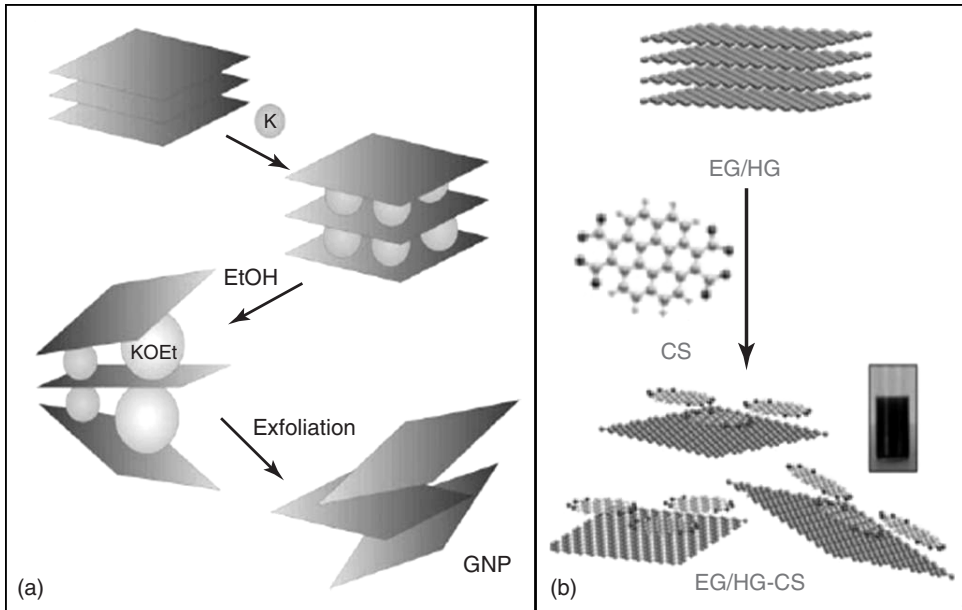


Figure 1.3 (a) Schematic diagram showing the intercalation of potassium between layers followed by violent reaction with alcohol to produce exfoliated ~ 30 layers of thin slabs of graphite. (Source: Reprinted with permission from Ref. [43].) (b) A schematic

illustration of the exfoliation of few-layer graphene with coronene tetracarboxylate (CS) to yield monolayer graphene–CS composites. (Source: Reprinted with permission from Ref. [45].)

also used to disperse graphene in perfluorinated aromatic solvents [46], orthodichloro benzene [47], and even in low-boiling solvents such as chloroform and isopropanol [48]. Hernandez *et al.* [49] carried out a detailed study on dispersibility of graphene in 40 different solvents and proposed that good solvents for graphene are characterized by the Hildebrand and Hansen solubility parameters. Greater than 63% of observed flakes had less than five layers in most solvents. Direct exfoliation and noncovalent functionalization and solubilization of graphene in water are achieved using the potassium salt of coronene tetracarboxylic acid (CS) to yield monolayer graphene–CS composites (Figure 1.3b) [45]. Stable high-concentration suspensions of FG were obtained by direct sonication in ionic liquids [50]. Exfoliation, reintercalation, and expansion of graphite yields highly conducting graphene sheets suspended in organic solvents [39]. Gram quantities of SLG have been produced from ethanol and sodium [51]. Under solvothermal conditions, alcoholic solutions of the metal get saturated with the metal alkoxide, and at autogenerated pressures of around 10^{-2} bar, the free alcohol gets encapsulated into the metal alkoxide in a clathrate-like structure. This is then pyrolyzed to yield a fused array of graphene sheets, and sonicated to yield SLG.

1.2.3

Chemical Vapor Deposition

The most promising, inexpensive, and readily accessible approach for the deposition of reasonably high quality graphene is CVD onto transition-metal substrates such as Ni [52], Pd [53], Ru [54], Ir [55], and Cu [56]. The process is based on the carbon saturation of a transition metal on exposure to a hydrocarbon gas at high temperature. While cooling the substrate, the solubility of carbon in the transition metal decreases and a thin film of carbon is thought to precipitate from the surface [57]. Different hydrocarbons such as methane, ethylene, acetylene, and benzene were decomposed on various transition-metal substrates such as Ni, Cu, Co, Au, and Ru [57].

A radio frequency plasma-enhanced chemical vapor deposition (PECVD) system has been used to synthesize graphene on a variety of substrates such as Si, W, Mo, Zr, Ti, Hf, Nb, Ta, Cr, 304 stainless steel, SiO₂, and Al₂O₃. This method reduces energy consumption and prevents the formation of amorphous carbon or other types of unwanted products [58–60]. Graphene layers have been deposited on different transition-metal substrates by decomposing hydrocarbons such as methane, ethylene, acetylene, and benzene. The number of layers varies with the hydrocarbon and reaction parameters. Nickel and cobalt foils that measure 5 × 5 mm² in area and 0.5 and 2 mm in thickness, respectively, have been used to carry out the CVD process at around 800–1000 °C; with nickel foil, CVD is carried out by passing methane (60–70 sccm) or ethylene (4–8 sccm) along with a high flow of hydrogen (around 500 sccm) at 1000 °C for 5–10 min. With benzene as the hydrocarbon source, benzene vapor diluted with argon and hydrogen was decomposed at 1000 °C for 5 min. On a cobalt foil, acetylene (4 sccm) and methane (65 sccm) were decomposed at 800 and 1000 °C, respectively. In all these experiments, the metal foils were cooled gradually after the decomposition. Figure 1.4 shows high-resolution TEM images of graphene sheets obtained by CVD on a nickel foil. Figure 1.4a shows graphenes obtained by the thermal decomposition of methane on the nickel foil, whereas Figure 1.4b shows graphene obtained by thermal decomposition of benzene. The insets in Figure 1.4a,b show selected area electron diffraction (SAED) patterns [61, 62]. All these graphene samples show G-band at 1580 cm⁻¹ and 2D band around 2670 cm⁻¹, with a narrow line width of 30–40 cm⁻¹. Figure 1.4c (i,ii) shows the Raman spectra of the graphene samples in Figure 1.4a,b, respectively. The narrow line width and relatively high intensity of the 2D-band confirm that these Raman spectra correspond to graphenes having one to two layers [57]. Graphene obtained by CVD process can be transferred to other substrates by etching the underlying transition metal and can be transformed into any arbitrary substrate.

1.2.4

Arc Discharge

Synthesis of graphene by the arc evaporation of graphite in the presence of hydrogen has been reported [61, 63]. This procedure yields graphene arc discharge graphene in H₂ atmosphere (HG) sheets with two to three layers having flake

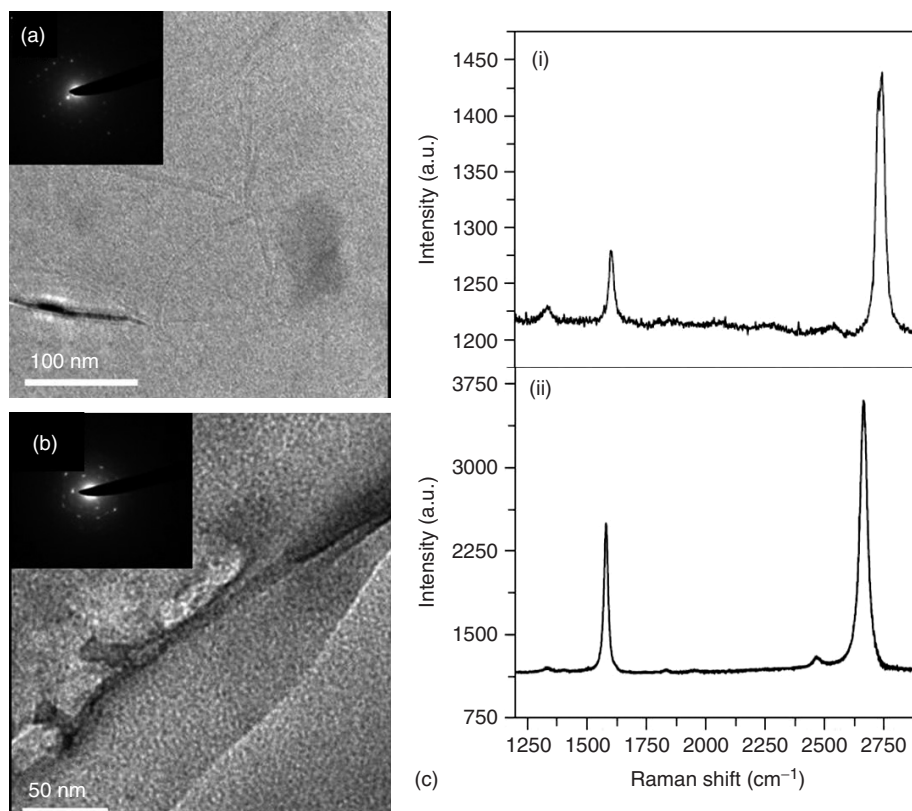


Figure 1.4 TEM images of graphene prepared by the thermal decomposition of (a) methane (70 sccm) at 1000 °C and (b) benzene (Ar passed through benzene with flow rate of 200 sccm) at 1000 °C on a nickel sheet. Insets show electron

diffraction pattern from the corresponding graphene sheets, and (c) the Raman spectra of graphene prepared from the thermal decomposition of (i) methane and (ii) benzene. (Source: Reprinted with permission from Ref. [61].)

size of 100–200 nm. This makes use of the knowledge that the presence of H_2 during arc discharge process terminates the dangling carbon bonds with hydrogen and prevents the formation of closed structures. The conditions that are favorable for obtaining graphene in the inner walls are high current (above 100 A), high voltage (>50 V), and high pressure of hydrogen (above 200 Torr). In Figure 1.5a,b, TEM and AFM images of HG sample are shown, respectively. This method has been conveniently used to dope graphene with boron and nitrogen [64]. To prepare boron-doped graphene (B-HG) and nitrogen-doped graphene (N-HG), the discharge is carried out in the presence of H_2 + diborane and H_2 + pyridine or ammonia, respectively. Later, based on these observations, some modifications in the synthetic conditions also yielded FG in bulk scale. Cheng *et al.* [65] used hydrogen arc discharge process as a rapid heating method to prepare graphene from GO. Arc discharge in an air atmosphere resulted in graphene nanosheets that

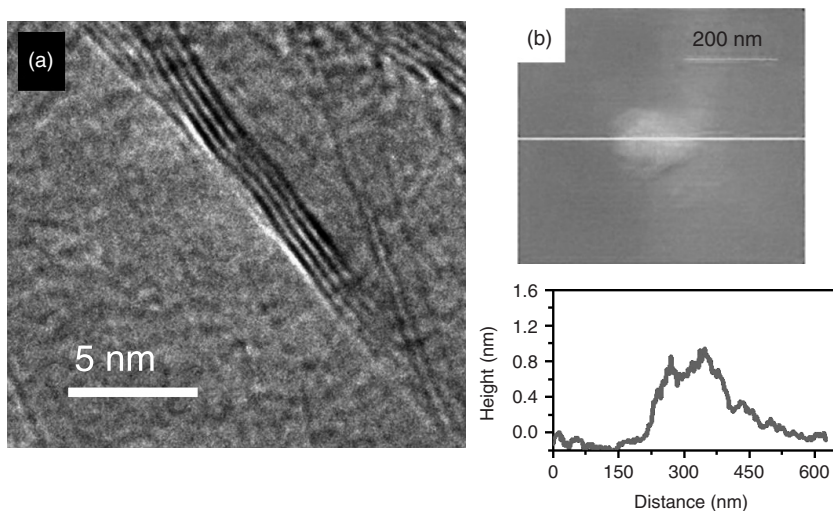


Figure 1.5 (a) TEM and (b) AFM image of HG prepared by arc discharge of graphite in hydrogen. Below is the height profile for the same. (Source: Reprinted with permission from Ref. [63].)

are ~ 100 – 200 nm wide predominantly with two layers. The yield depends strongly on the initial air pressure [66]. Li *et al.* [67] have synthesized N-doped multilayered graphene in He and NH_3 atmosphere using the arc discharge method. Arc discharge carried out in a helium atmosphere has been explored to obtain graphene sheets with different number of layers by regulating gas pressures and currents [68].

1.2.5

Reduction of Graphite Oxide

Chemical reduction of graphite oxide is one of the established procedures to prepare graphene in large quantities [33]. Graphite oxide when ultrasonicated in water forms a homogeneous colloidal dispersion of predominantly SGO in water. RGO with properties similar to that of graphene is prepared through chemical, thermal, or electrochemical reduction pathways [69]. While most strong reductants have slight reactivity with water, hydrazine monohydrate does not, making it an attractive option for reducing aqueous dispersions of graphene oxide [70]. Syn addition of H_2 occurs across the alkenes, coupled with the extrusion of nitrogen gas. Large excess of NaBH_4 has also been used as a reducing agent [71]. Other reducing agents used include phenyl hydrazine [72], hydroxylamine [73], glucose [74], ascorbic acid [75], hydroquinone [76], alkaline solutions [77], and pyrrole [78]. Electrochemical reduction is another means to synthesize graphene in large scale [79–81]. The reduction initiates at -0.8 V and is completed by -1.5 V, with the formation of black precipitate onto the bare graphite electrode. Zhou *et al.* [82] coupled electrochemical reduction with a spray coating technique to prepare large-area and patterned RGO films with thicknesses ranging from a single

monolayer to several micrometers on various conductive and insulating substrates. Organic dispersions of graphene oxide can be thermally reduced in polar organic solvents under reflux conditions to afford electrically conductive, chemically active reduced graphene oxide (CARGO) with tunable C/O ratios, dependent on the boiling point of the solvent. The dispersing medium must have a boiling point above 150 °C (the initiation point of the mass loss feature in the thermogravimetric analysis (TGA) profile of graphene oxide) and be able to disperse both graphene oxide and CARGO, for example, DMF, dimethyl sulfoxide, and NMP have been used for the purpose [81].

Photothermal and photochemical reduction of GO is a rapid, clean, and versatile way to form RGO. Ding *et al.* [83] reduced GO using UV irradiation to obtain single- to few-layered graphene sheets without the use of any photocatalyst. Cote *et al.* [84] prepared RGO by photothermal reduction of GO using xenon flash at ambient conditions and patterned GO or GO/polymer films using photomask. Nanosecond laser pulses of KrF excimer laser or 335 and 532 nm were shown to effectively reduce dispersions of GO to thermally and chemically stable graphene [85]. High-quality RGO has been prepared by irradiating GO with sunlight, ultraviolet light, and KrF excimer laser [61]. The reduction of GO to graphene by excimer laser irradiation results in the change of color of the solid GO film from brownish yellow to black. (Figure 1.6 shows darkening on reduction). Carbonyl and other oxygen functionalities on the surface of the GO film nearly disappear after irradiation, as can be seen from the infrared spectra shown in Figure 1.6a,b. The electrical conductivity increases by 2 orders of magnitude after laser irradiation of the GO film as shown in Figure 1.6c. Photochemical reduction of GO and SGO to graphene has also been exploited for patterning. For this purpose, GO films deposited on Si substrates were subjected to excimer laser radiation (Lambda Physik KrF excimer laser, 248 nm wavelength, 30 ns lifetime, 300 mJ laser energy, 5 Hz repetition rate, 200 shots), after inserting a TEM grid as the mask and covering them with a quartz plate [86, 87]. Figure 1.7a shows a schematic representation of the process of laser patterning using TEM grid as mask, and Figure 1.7b shows the optical microscopic image of the pattern achieved after excimer laser reduction of graphene oxide. Electron-beam-induced reduction of GO has been reported [88]. Electron-beam patterning of GO films has been used to obtain patterns of RGO as thin as 240 nm, as shown in Figure 1.7c [87].

Graphene oxide can be reversibly reduced and oxidized using electrical stimulus. Controlled reduction and oxidation in two-terminal devices containing multilayer graphene oxide films was demonstrated by Ekiz *et al.* [89] and by Yao *et al.* [90]. Microwave irradiation (MWI)-induced heating has been used as a rapid way to synthesize graphene sheets. Owing to the difference in the solvent and reactant dielectric constants, selective dielectric heating can provide significant enhancement in the transfer of energy directly to the reactants, which causes an instantaneous internal temperature rise and thereby reduction of GO [91]. Dry GO absorbs MWI strongly with a sudden increase in surface temperature of the GO, up to ~400 °C, within just 2 s, leading to an ultrafast reduction of GO to RGO [92].

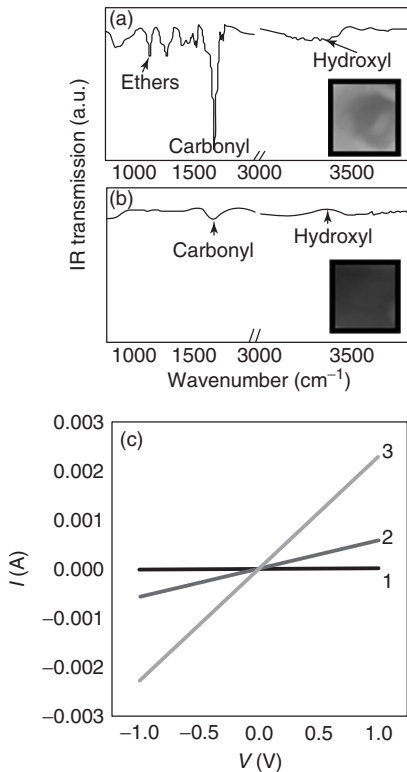


Figure 1.6 FTIR spectra of GO (a) before and (b) after laser reduction (laser reduced graphene oxide, LRG0). Insets show photographs of GO before and after reduction, respectively. (c) Current–voltage characteristics of 1, GO; 2, LRG0; 3, LRG0-Pt. (Source: Reprinted with permission from Ref. [87].)

1.3 Synthesis of Graphene Nanoribbons

Graphene nanoribbons (GNRs) can be thought of as thin strips of graphene or unrolled CNTs. GNRs have attracted attention because of their novel electronic and spin transport properties [5, 93–95]. GNRs of width 10–100 nm and 1–2 μm were prepared for the first time by oxygen plasma etching of graphene sheets [96]. A negative tone e-beam resist, hydrogen silsesquioxane (HSQ), is used to protect the underlying graphene layer, while the unprotected layer gets etched away by the oxygen plasma [96]. Tapaszto *et al.* [97] etched geometrically and crystallographically oriented GNRs from graphene sheets by applying constant bias potential (higher than that used for imaging) and simultaneously moving the STM tip with constant velocity over the surface. These methods did not produce GNRs of widths less than 20 nm and had edge roughness of ~ 5 nm. Li *et al.* [93] chemically prepared sub-10 nm width GNRs of varying lengths from thermally exfoliated graphite by dispersing it in a 1,2-dichloroethane (DCE) solution of poly(*m*-phenylenevinylene-co-2,5-dioctoxy-*p*-phenylenevinylene) (PmPV) by sonication and removing the larger pieces by centrifugation. Cano-Marquez *et al.* [98] prepared 20–300 nm few-layered GNRs in bulk scale by CVD of ethanol, with ferrocene and thiophene acting as catalysts.

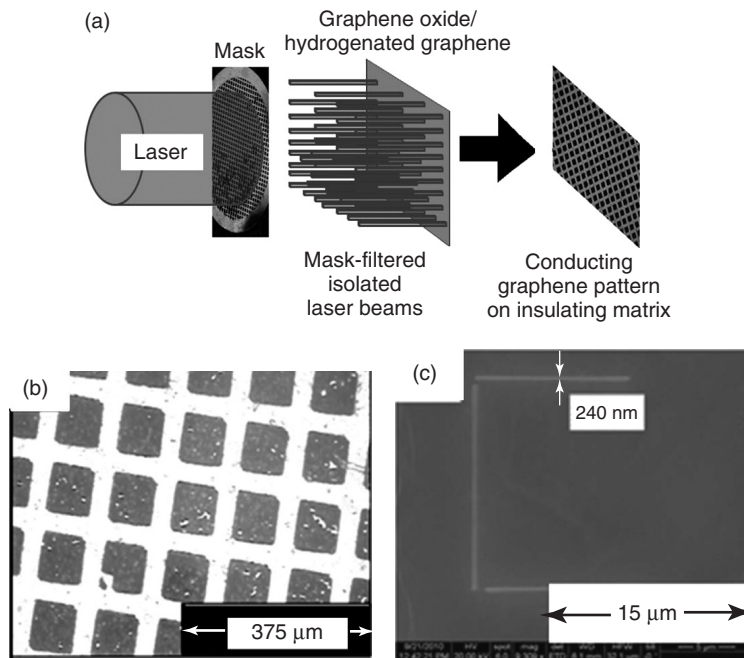


Figure 1.7 (a) Schematic diagram illustrating masked laser patterning. (Source: Reprinted with permission from Ref. [86].) (b) Optical microscopic image of the pattern achieved after excimer laser reduction of

graphene oxide, and (c) electron-beam pattern with 240 nm wide lines of RGO on GO films. (Source: Reprinted with permission from Ref. [87].)

Longitudinal unzipping of CNTs has been used for synthesis of GNRs. While Kosynkin *et al.* [99] carried out oxidative unzipping using $\text{KMnO}_4/\text{H}_2\text{SO}_4$ mixture, Higginbotham *et al.* [100] used a second acidlike trifluoroacetic acid (TFA) or H_3PO_4 to get more controlled oxidation (protection of the vicinal diols formed on the basal plane of graphene during the oxidation, thereby preventing their overoxidation to diones and the subsequent hole generation), yielding high-quality GNRs with lesser holes. Figure 1.8a shows a schematic of potassium intercalation and sequential longitudinal splitting of the CNT walls to yield a nanoribbon stack. Jiao *et al.* [101] carried out mild gas-phase oxidation to create defects on CNTs that were then dispersed in DCE solution of PmPV by sonication and obtained high-quality unzipped nanoribbons. Cano-Marquez *et al.* [98] and Kosynkin *et al.* [102] unzipped CNTs by alkali metal intercalation and exfoliation either by protonation or with acid treatment and abrupt heating. Jiao *et al.* [103] carried out controlled unzipping of partially embedded CNTs in poly(methyl methacrylate) (PMMA) by Ar plasma etching. GNRs have also been obtained by sonochemical cutting of graphene sheets involving oxygen-induced unzipping of graphene sheets [104]. Laser irradiation of undoped and doped multiwalled CNTs by an excimer laser (energy $\sim 200\text{--}350$ mJ) also yielded GNRs (Figure 1.8b) [105].

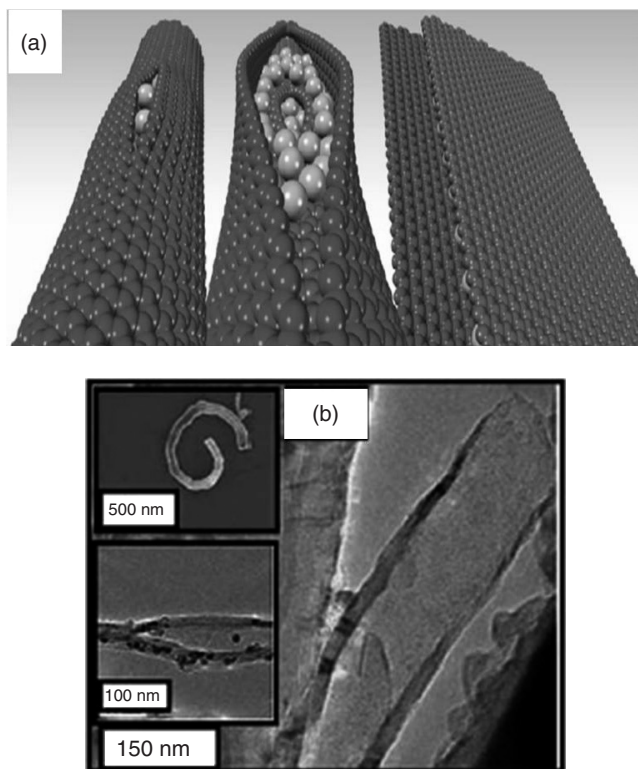


Figure 1.8 (a) Schematic of the splitting process produced by potassium intercalation between the nanotube walls and sequential longitudinal splitting of the walls followed by unraveling to a nanoribbon stack. (Source: Reprinted with permission from Ref. [44].) (b) Boron-doped CNT irradiated

with laser energy of 250 mJ. Top inset shows the corresponding FESEM (field emission scanning electron microscopic) image. Bottom inset shows a TEM image of partially opened boron-doped CNT irradiated at 200 mJ. (Source: Reprinted with permission from Ref. [105].)

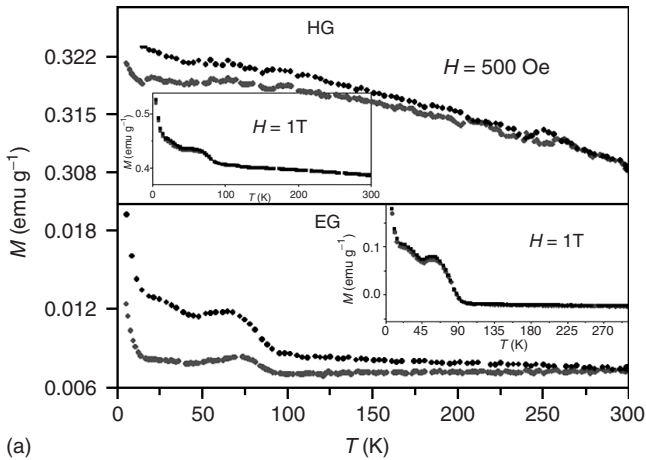
GNRs have also been obtained by PECVD on Pd nanowire templates. On removing the Pd nanowires, tubular graphene layer collapsed to yield edge-closed nanoribbons, while the graphene layers on the top part of the metal nanowire were selectively etched by O_2 plasma to yield edge-opened GNRs [106]. Wang and Dai [107] prepared 20–30 nm wide GNR arrays lithographically and used gas-phase etching chemistry to narrow the ribbons down to <10 nm, thereby achieving a high on/off ratio up to $\sim 10^4$. Bottom-up fabrication provides precise control over topologies and widths of GNRs. Surface-assisted coupling of molecular precursors into linear polyphenylenes and their subsequent cyclodehydrogenation have been used to prepare GNRs with predefined edge structure and morphology [108]. Yang *et al.* [109] carried out the Suzuki–Miyaura polymerization of the bis-boronic esters with diiodobenzenes to prepare polyphenylenes resembling GNRs.

1.4 Selected Properties

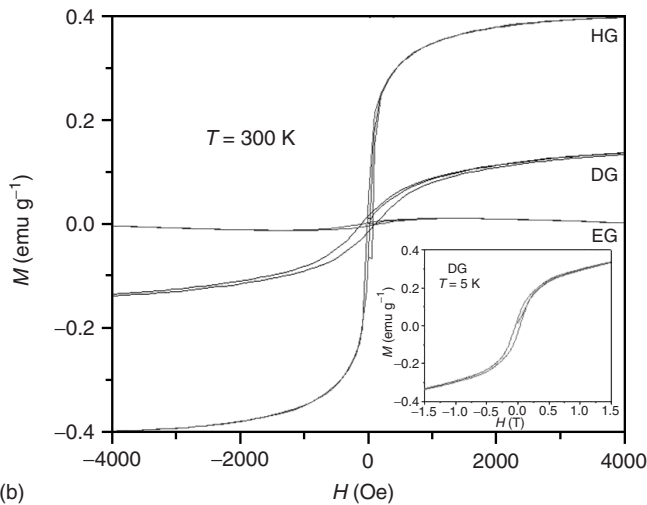
1.4.1 Magnetic Properties

Occurrence of high-temperature ferromagnetism (FM) in graphite-related materials is a topic of considerable interest. Yazyev *et al.* [110] showed that magnetism in graphene can be induced by vacancy defects or by hydrogen chemisorption. Some workers suggest that the zig-zag edges are responsible for the magnetic properties of graphene [111]. Inhomogeneous distribution of FM structures of nanographene sheets has been observed below 20 K [112]. Microporous carbon exhibits high-temperature FM originating from topological disorder associated with curved graphene [113]. Nanosized diamond particles implanted with nitrogen and carbon show FM hysteresis at room temperature [114]. Wang *et al.* [8] reported room temperature FM in a graphene sample prepared by the partial reduction of graphene oxide with hydrazine followed by annealing the samples at different temperatures in an argon atmosphere. Magnetic properties of graphene samples prepared by EG, conversion of nanodiamond (DG), and arc evaporation of graphite in hydrogen (HG) have been studied. The number of graphene layers in EG, DG, and HG was estimated to be six to seven, four to five, and two to three, respectively [3, 9, 61]. All these samples show divergence between the field-cooled (FC) and zero-field-cooled (ZFC) data, starting around 300 K. In Figure 1.9a, we show the temperature dependence of magnetization of EG and HG samples measured at 500 Oe. The divergence nearly disappears on application of 1 T as can be seen from the insets in Figure 1.9a. The divergence between the FC and ZFC data in the graphene samples is comparable to that in magnetically frustrated systems such as spin glasses and superparamagnetic materials. The Curie–Weiss temperatures obtained from the high-temperature inverse susceptibility data were negative in all these samples, indicating the presence of antiferromagnetic interactions. Interestingly, we observe well-defined maxima in the magnetization at low temperatures, the maxima becoming prominent in the data recorded at 1 T (see insets in Figure 1.9a). Such magnetic anomalies are found when antiferromagnetic correlations compete with FM order. Application of high fields can align the FM clusters and decrease the divergence between FC and ZFC data, as indeed observed. It is possible that the data correspond to percolation type of situation, wherein different types of magnetic states coexist. The FM clusters in such a case would not be associated with a well-defined global FM transition temperature. This behavior is similar to that of microporous carbon and some phase-separated members of the rare earth manganite family, $\text{Ln}_{1-x}\text{A}_x\text{MnO}_3$ (Ln = rare earth, A = alkaline earth) [115, 116]. Theoretical calculations predict the presence of antiferromagnetic states in the sheets and FM states at the edges of graphene [117].

The graphene samples show magnetic hysteresis at room temperature (Figure 1.9b) and the M_S increases with increase in temperature. Of the three samples, HG shows the best hysteretic features with saturation. While DG shows



(a)



(b)

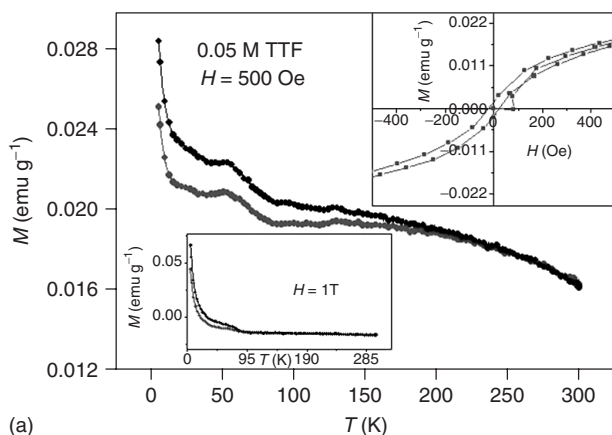
Figure 1.9 (a) Temperature variation of magnetization of few-layer graphenes EG and HG at 500 Oe, showing the ZFC and FC data. The insets show the magnetization data at 1 T. (b) Magnetic hysteresis in EG, DG, and HG at 300 K. Inset shows magnetic hysteresis in DG at 5 K. (Source: Reprinted with permission from Ref. [9].)

saturation magnetization, M_S , it is low when compared to HG. We see that θ_p , M_R , and M_S are the highest in case of HG, which also shows a higher value of magnetization than the other samples at all temperatures. The values of the various magnetic properties of the samples (M_S at 300 K) are plotted in Figure 1.9b to demonstrate how the properties vary as $\text{HG} > \text{DG} > \text{EG}$. It is noteworthy that both the area and the number of layers vary in the order of $\text{EG} > \text{DG} > \text{HG}$. It is likely that edge effects would be greater in samples with a smaller number of layers as well as small areas. In the case of HG, hydrogenation occurred to some extent, thereby favoring FM. Magnetic properties of DG samples prepared

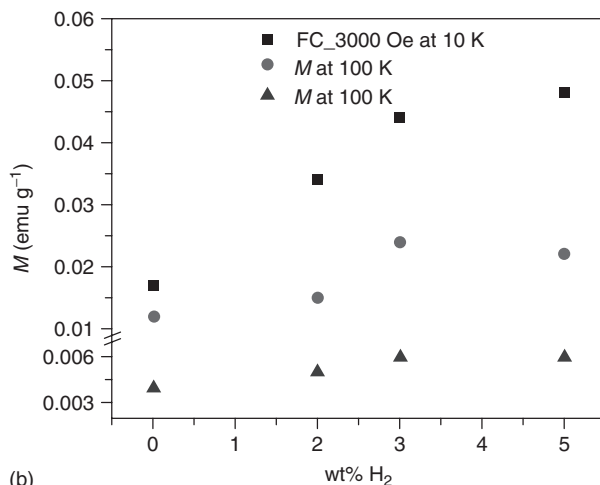
at different temperatures show a systematic decrease in magnetization with increase in the temperature of preparation. Electron paramagnetic resonance (EPR) measurements in the 2.5–300 K range on EG, DG, and HG show a signal with a line width of 0.7–2.9 mT and a g -value in the 2.006–2.013 range. The small value of the line width and the small deviation in the g -value from the free-electron value suggest that the spins do not originate from transition-metal impurities but from the spin species in the graphene sheets.

Adsorption of different guest molecules on graphene gives rise to a reversible low-spin/high-spin magnetic switching phenomenon, which depends on the nature of the guest species. Adsorption of H₂O [118], interaction with acids [119], and intercalation with potassium clusters reduce the magnetization of nanographite [120]. The reduction in magnetization has been interpreted as due to the interaction with lone pair orbitals as well as charge transfer with graphene sheets. The edge sites participating in host–guest interactions can give rise to magnetic phenomenon. Guest molecules accommodated through physisorption mechanically compress the flexible nanographite domains, leading to a significant reduction in the internanographene-sheet distance. Such a reduction in the intersheet distance could align the magnetic moments antiparallely and reduce the net magnetic moment [121]. Adsorption of benzene solutions of tetrathiafulvalene (TTF) and tetracyanoethylene (TCNE) is found to profoundly affect the magnetic properties of FG. In Figure 1.10a, we show typical results on the effect of adsorbing 0.05 M solution of TTF on the magnetic properties of HG. The value of the magnetization drastically decreases on adsorption of TTF and TCNE, although the basic trend in the temperature variation of magnetization remains the same. Thus, the graphene sample continues to show room-temperature hysteresis. On increasing the concentration of TTF or TCNE, the magnetization value decreases progressively. Interestingly, TTF has a greater effect than TCNE, even though the magnitude of adsorption of TCNE on HG is greater. The value of M_S at 300 K decreases on adsorption of TTF and TCNE, the decrease being larger in the case of former. Clearly, charge-transfer interaction between graphene and TTF (TCNE) [13] is responsible for affecting the magnetic properties. The reversible concentration-dependent effects of TTF and TCNE on the magnetic properties of graphene support the idea that the magnetic properties of the graphene samples are intrinsic.

Hydrogenation of graphene can induce magnetism since the formation of tetrahedral carbons can reduce the connectivity of the π -sheets and the π – π energy gap of the localized double bonds and hence the ring current diamagnetism. Such changes in structure can therefore cause an increase in magnetic susceptibility [122]. Hydrogenated graphene samples with varying hydrogen contents have been prepared using the Birch reduction [123]. The samples of 2, 3, and 5 wt%, designated HGH_1, HGH_2, and HGH_3 respectively, have been examined for their magnetic properties. We observe a gradual increase in the magnetic moment, with an increase in the hydrogen content. An anomaly is also observed in magnetism from 50 to 80 K in the case of ZFC of HGH_2 when compared to HG probably due to percolation type of situation arising from different types of magnetic states. It appears that there is a change in the magnetic structure in HGH_2 compared to HG. In



(a)



(b)

Figure 1.10 (a) Temperature variation of the magnetization of the few-layer graphene HG (500 Oe) after adsorption of 0.05 M solution of TTF. The magnetization data given in the figure are corrected for the weight of adsorbed TTF. Magnetic hysteresis data at 300 K and magnetization data at 1 T are shown in the insets. Magnetization data of HG with adsorbed TCNE are similar to

those with TTF, except that the decrease in magnetization relative to pure HG is much smaller. (Source: Reprinted with permission from Ref. [9].) (b) Comparison of the magnetic properties of the hydrogenated few-layer graphene HG: HGH_1, HGH_2, and HGH_3. (Source: Reprinted with permission from Ramakrishna Matte *et al. Chem. Sci*, doi: 10.1039/c1sc00726b.)

Figure 1.10b, the remanent magnetization (M_r), saturation magnetization (M_s), and magnetization at 3000 Oe (FC at 10 K) of HG with different weight percentages of hydrogen are shown. The values of these properties increase with hydrogen content. On dehydrogenation at 500 °C for 4 h, the samples exhibit a decrease in the magnetic moment. This observation confirms that the increase in the magnetic

properties is due to hydrogenation. On dehydrogenation, the hydrogenated samples revert to the initial graphene samples.

1.4.2

Electrical Properties

Intrinsic graphene is a semimetal or a zero-gap semiconductor. FGs show semiconducting nature, with the resistivity showing little change in the 100–300 K range. Conductivity, on the other hand, shows a sharp increase from 35 to 85 K, and the slope of temperature versus conductivity curve reduces thereafter. Resistance of FG decreases markedly if it is heated to high temperatures. Resistivity decreases markedly with increase in the number of layers as demonstrated by EG, HG, and RGO (ρ of RGO < HG < EG) samples with three to four layers, two to three layers, and single layer, respectively. Room-temperature thermal conductivity of graphene has been measured using a noncontact optical technique. The conductivity of graphene goes up to $(5.30 \pm 0.48) \times 10^3 \text{ W mK}^{-1}$ outperforming CNTs [4]. Experiments with field-effect transistors (FETs) on micromechanically cleaved graphene by Novoselov *et al.* [1] have revealed that the sheet resistivity (ρ depends on the gate voltage (V_g)) exhibits a sharp peak to a value of several kilohms and decays back to 100Ω on increasing V_g (Figure 1.11a). At the same V_g where ρ had its peak, the Hall coefficient showed a sharp reversal of its sign, thus revealing ambipolar character (Figure 1.11b). FET characteristics of EG, DG, HG, N-HG, and B-HG have been investigated by us in comparison with RGO, and RGO showed ambipolar transfer characteristics on sweeping the V_{gs} between -20 and $+20$ V and V_{ds} at 1 V (Figure 1.12a), while all the FGs showed n-type behavior. The highest mobility was found with HG possessing two to three layers and with the least defects. FETs based on B-HG and N-HG show n-type and p-type behavior, respectively (Figure 1.12b,c) [124]. Novoselov's micromechanically cleaved graphene showed extremely high mobilities of $\sim 15000 \text{ cm}^2 (\text{V s})^{-1}$ at room temperature with electron and hole concentrations of 10^{13} cm^{-2} with ballistic transport up to submicrometer distances [1]. Two- to three-layered HG samples have shown mobilities of $10\,428 \text{ cm}^2 (\text{V s})^{-1}$, while all other few-layered samples showed much lower mobilities [125]. Different factors such as the average number of layers, surface functionality, and concentration of defects are found to be responsible for observing different characteristics in different samples. HG with the smallest number of layers exhibits the highest mobility. It is remarkable that transistor characteristics are found even in few-layer samples with defects [61]. The linear dispersion relation of graphene predicts that the resistivity of graphene due to isotropic scatterers is independent of the carrier density. Hwang and Das Sarma [126] theoretically calculated the phonon-scattering-limited extrinsic electron mobility in graphene to be a function of temperature and carrier density, with the room-temperature intrinsic mobility reaching the values of above $10^5 \text{ cm}^2 (\text{V}\cdot\text{s})^{-1}$. Chen *et al.* [4] have shown that electroacoustic phonon scattering in graphene is independent of the carrier density and contributes just 30Ω to room temperature resistivity of graphene, with the intrinsic mobility of graphene being $200\,000 \text{ cm}^2 (\text{V}\cdot\text{s})^{-1}$. The

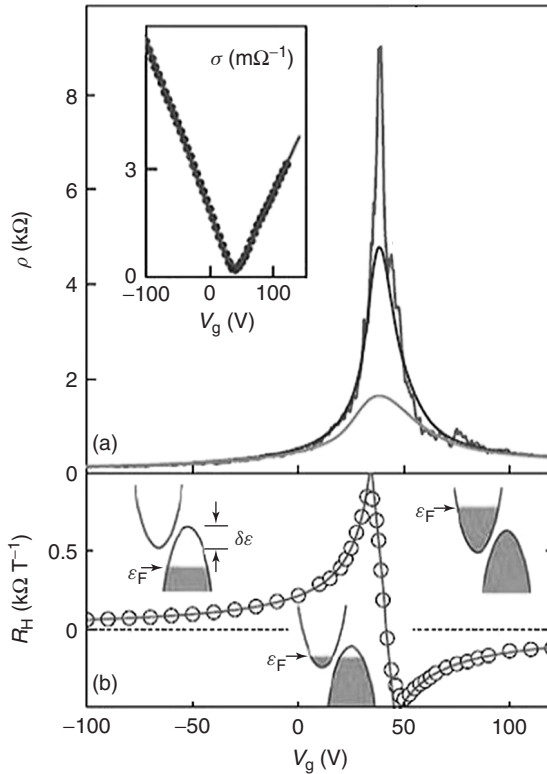


Figure 1.11 (a) Resistivity ρ of few-layer graphene on gate voltage (V_g) for different temperatures ($T = 5, 70,$ and 300 K from top to bottom), with the inset showing the change in conductivity $\sigma = 1/\rho$ (at 70 K). (b) The Hall coefficient R_H versus V_g for the same at 5 K. (Source: Reprinted with permission from Ref. [1].)

actual mobility is, however, dependent on scattering by various extrinsic factors such as surface phonons [4, 125–128], charged impurities on top of graphene or in the underlying substrate [128, 129], and ripples and corrugation in the graphene sheet [130]. Dramatically reduced carrier scattering was reported in suspended graphene devices by Du *et al.* [131] allowing the observation of a very high mobility of $120\,000\text{ cm}^2 (\text{V}\cdot\text{s})^{-1}$ near room temperature ($T \sim 240$ K).

Since the band gap of graphene is 0, devices with channels made of large-area graphenes cannot be switched off and therefore are not suitable for logic applications. However, the band structure of graphene can be modified to open a band gap by constraining large-area graphene in one dimension to form GNRs. Han *et al.* [5] first investigated electronic transport in lithographically patterned graphene ribbons and demonstrated band gap opening due to lateral confinement of charge carriers in case of narrower nanoribbons; band gap increases with decrease in nanoribbons' width. The sizes of these energy gaps were investigated by measuring the conductance in the nonlinear response regime at low temperatures [132]. Chen *et al.* [96]

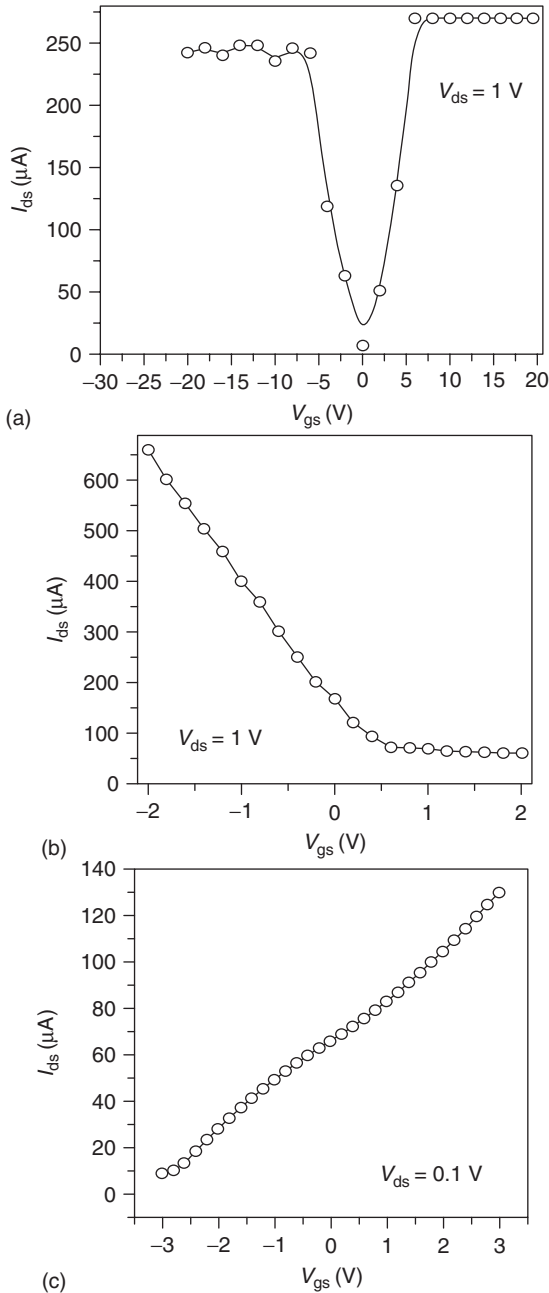


Figure 1.12 Transfer characteristics (I_{ds} vs V_{gs}) of FETs based on (a) RGO, (b) B-HG, and (c) N-HG. Here, I_{ds} , V_{ds} , and V_{gs} stand for source to drain current, source to drain voltage, and gate to source voltage, respectively. (Source: Reprinted with permission from Ref. [124].)

have fabricated GNR FETs with 20–40 nm width and measured FET characteristics and ON/OFF ratios. FETs with sub-10 nm nanoribbons prepared by Wang *et al.* [94] showed much greater $I_{\text{ON}}/I_{\text{OFF}}$ of 10^5 at room temperature. The device had 20 times higher current density and 100 times higher transconductance per micrometer due to the larger band gaps and high GNR quality with better edge smoothness.

Graphene is considered to be the next-generation electrode material due to its extraordinary thermal, chemical, and mechanical stability. Transparent conducting films made of RGO have been fabricated [133]. These films are similar to HOPG in electronic and structural properties. Graphene films prepared by direct CVD on Ni substrates have been transferred onto polyethylene terephthalate (PET) substrate (thickness, 100 μm) coated with a thin polydimethylsiloxane (PDMS) layer (thickness, 200 μm) to prepare flexible, stretchable, foldable, transparent (80% optical transparency), conducting (sheet resistance of only $\sim 280 \Omega$ per square) films [52]. Conductivity as a function of bending radii has been studied and results hold promise for the application of these films as highly conducting, macroscopic, flexible transparent conducting electrodes. Mak *et al.* [134] studied optical reflectivity and transmission properties of graphene over photon energies of 0.2 and 1.2 eV and explained the properties based on the noninteracting massless Dirac fermions.

Band structure of graphene can be tuned by confining it to one dimension, as in the case of GNRs, to generate highly spin-polarized currents [135]. Bai *et al.* [136] obtained almost 100% magnetoresistance at low temperatures, with almost 50% remaining at room temperature for GNRs fabricated using the nanowire etch mask technique [137]. Such high magnetoresistance devices can find use in spin valve devices. Graphene-based superconducting transistors were reported by Heersche *et al.* [138] Although graphene is not superconducting by itself, it shows supercurrents over short distances when placed between superconducting electrodes because of the Josephson effect. Using the nonequilibrium Green's function method, transmission of superconductor-graphene-superconductor junctions has been examined theoretically and the possibility of superconducting switch has been predicted [139]. Palladium sheets sandwiched between graphene sheets give rise to a superconducting transition around 3.6 K [140]. Superconductivity here occurs in the Pd sheets.

1.4.2.1 Supercapacitors

Electrochemical properties of a few graphenes prepared by different methods have been investigated using the redox reactions with potassium ferrocyanide [141]. Among EG, DG (see Section 4.1 for description), and a graphene prepared by CVD over Ni and Co foils (CG), EG shows a behavior similar to the basal plane in graphite, whereas DG and CG show slightly better kinetics. Vivekchand *et al.* [142] prepared electrochemical supercapacitors with different graphene samples as electrode materials in aqueous H_2SO_4 as well as in an ionic liquid (*N*-butyl-*N*-methylpyrrolidinium bis(trifluoromethanesulfonyl)imide, PYR14TFSI) that were used as electrolytes. EG and DG exhibit high specific capacitance in aqueous H_2SO_4 , the value reaching up to 117 and 35 F g^{-1} , respectively. Voltammetric characteristics of a capacitor built from graphene electrodes (5 mg each), at a scan

rate of 100 mV s^{-1} using aqueous H_2SO_4 (1 M) (Figure 1.13a,b), show specific capacitance as a function of scan rate for different graphene samples. Using an ionic liquid, the operating voltage has been extended to 3.5 V (instead of 1 V in the case of aqueous H_2SO_4), the specific capacitance values being 75 and 40 F g^{-1} for EG and DG, respectively. High-surface-area graphite prepared by ball milling showed a large specific capacitance of $33 \mu\text{F cm}^{-2}$ in aqueous medium, which might be due to high open surface area, lattice defects, and oxygen functional groups in the sample [143].

Chemically modified graphene sheets obtained by the reduction of graphene oxide with hydrazine when used as electrode material in supercapacitors gave specific capacitances of 135 and 99 F g^{-1} in aqueous and organic electrolytes, respectively [144]. 3D CNT/graphene sandwich structures with CNT pillars grown in between the graphene layers have been used as high-performance electrode materials for supercapacitors, and a maximum specific capacitance of 385 F g^{-1} could be obtained

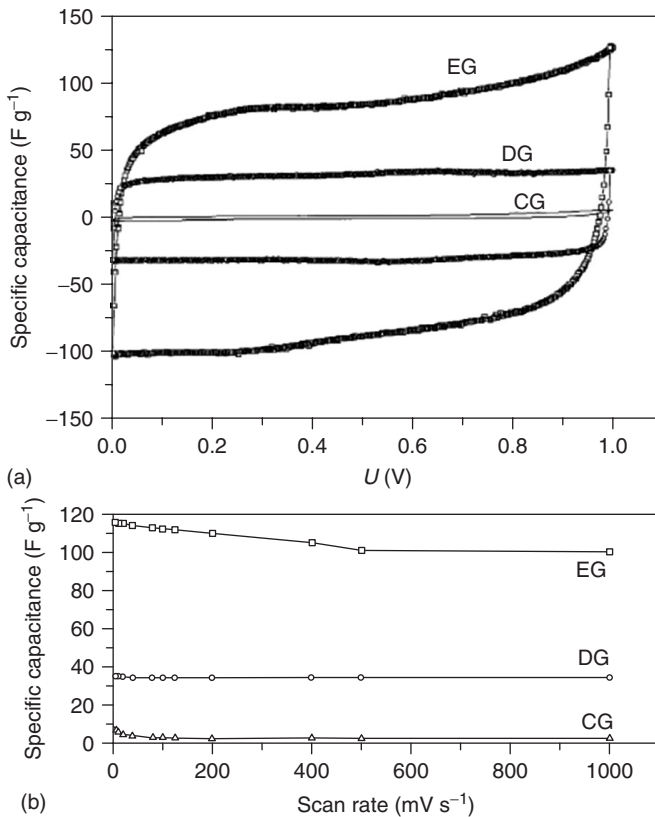


Figure 1.13 (a) Voltammetric characteristics of a capacitor built from different graphene electrodes (5 mg each) at a scan rate of 100 mV s^{-1} in aqueous H_2SO_4 (1 M), and (b) specific capacitance as a function of scan rate. (Source: Reprinted with permission from Ref. [142].)

at a scan rate of 10 mV s^{-1} in 6 M KOH aqueous solution [145]. Some novel strategies to synthesize graphene-based nanocomposites containing polyaniline [146] and Co(OH)_2 [147], and so on, for enhancing the electrochemical capacitance aqueous solution have been explored. Graphene/polyaniline composites with an appropriate weight ratio prepared using *in situ* polymerization exhibited a higher specific capacitance of 1046 F g^{-1} at a scan rate of 1 mV s^{-1} due to the synergistic effect between graphene and polyaniline. Graphene/ Co(OH)_2 nanocomposite shows a capacitance as high as 972.5 F g^{-1} , leading to a significant improvement. Graphene nanosheets show high lithium storage capacity for lithium secondary batteries, the value reaching 540 mAh g^{-1} . This storage capacity can be further improved to 730 and 784 mAh g^{-1} , respectively, by incorporating CNTs and C60 [147].

1.4.2.2 Photovoltaics and Photodetectors

Photovoltaic devices fabricated with a bulk heterojunction (BHJ) architecture using solution-processible graphene as electron-acceptor material are reported. A power conversion efficiency of 14% is obtained using simulated 100 mW cm^{-2} AM 1.5G illumination [148]. The optical transparency and conductivity of graphene can be exploited for many photonic devices. For example, liquid-crystal devices with electrodes made of graphene show excellent performance with a high contrast ratio [149]. Conducting films of graphene for solar cell applications can also be prepared by a bottom-up approach [150]. Polymer photovoltaic cells based on solution-processible graphene are reported [151]. Because of its unique electronic structure, graphene shows useful photonic properties such as absorption of significant fraction of incident white light [6] and strong, tunable interband transitions [152]. Above $\sim 0.5 \text{ eV}$, absorbance of graphene is additive resulting in strong graphene–light interactions. This has made possible fabrication of FETs for ultrafast photodetection [153]. Solution-processed thin films prepared using GO enable easy material processing and mechanical flexibility, making them useful candidates for use in large-area devices.

GNRs with substantial gaps have been used as phototransistors [154], specially for far-infrared detection [155]. It has been possible to prepare highly selective, sensitive, and high-speed nanoscale photodetectors and photoelectronic switches by drop-casting RGO and GNR on two-terminal $15 \mu\text{m}$ gap Cr (5 nm)/Au (300 nm) electrodes [156]. Electrical conductivities of RGO and GNR increase with IR laser irradiation. An RGO detector can sense the IR radiation emitted from a human body. The *detector current responsivity* (R_λ), defined as the photocurrent generated per unit power of the incident light on the effective area of a photoconductor, and the external quantum efficiency (EQE), defined as the number of electrons detected per incident photon for RGO photoconductors, are 4 mA W^{-1} and 0.3%, respectively, whereas for GNR, these values are higher, being 1 A W^{-1} and 80%, respectively, for an incident wavelength of 1550 nm at 2 V. RGO and GNRs. On absorbing light from an IR source, electron–hole (e-h) pairs are generated [157] because of a barrier like the Schottky barrier at the metal/graphene contact. The e-h pairs generated in graphene would normally recombine on a timescale of tens of picoseconds, depending on the quality and carrier concentration of the graphene

[125, 157, 158]. On application of an external field, the pairs get separated and a photocurrent is generated. A similar phenomenon can occur in the presence of an internal field formed by photoexcitation [159–161]. Graphene is also a very good UV absorber [162]. It has been possible to prepare UV detectors using RGO. The photodetecting responsivity is found to be 0.12 A W^{-1} with an EQE of 40% [163].

1.4.2.3 Field Emission and Blue Light Emission

Recently, there have been several attempts to investigate field emission properties of graphene films [164–166]. To take advantage of the high field enhancement, graphene sheets would have to stand on their edges and not lay laterally flat on the substrate. A spin-coated graphene–polystyrene composite film was reported to exhibit a threshold field of $4 \text{ V } \mu\text{m}^{-1}$ (at $10^{-8} \text{ A cm}^{-2}$) with a field enhancement factor of 1200 [164]. Malesevic *et al.* [165] grew vertically aligned FG films by CVD and found these films to exhibit favorable turn-on field but decays after five cycles. Besides geometrical factors, spatial distribution can also tailor the work function and provide another means to improve electron field emission. Field emission properties of undoped arc-discharge-prepared graphene (HG), as well as B-HG and N-HG, have been studied. Electrophoretic deposition was used for depositing vertically oriented graphene sheets [167]. N-HG showed the lowest turn-on field of $0.6 \text{ V } \mu\text{m}^{-1}$ with an emission current density of $10 \mu\text{A cm}^{-2}$ (Figure 1.14a). Emission current was generally stable for almost 3 h or more.

Aqueous solutions of acid-treated graphene or RGO show blue emission centered at 440 nm on being excited by UV of 325 nm [169]. On mixing the blue-light-emitting graphene samples with the yellow-light-emitting zinc oxide nanoparticles, it is possible to get a bluish-white light as can be seen from the PL spectra in Figure 1.14b. A plausible cause of the blue photoluminescence in RGO is the radiative recombination of e-h pairs generated within localized states. The energy gap between the π - and π^* -states generally depends on the size [170] of the sp^2 clusters or the conjugation length [171]. Interaction between nanometer-sized sp^2 clusters and finite-sized molecular sp^2 domains could play a role in optimizing the blue emission in RGO. The presence of isolated sp^2 clusters in a carbon-oxygen sp^3 matrix can lead to the localization of e-h pairs, facilitating radiative recombination of small clusters.

1.4.3

Molecular Charge Transfer

Interaction of carbon nanostructures with electron-donor and electron-acceptor molecules causes marked changes in their electronic structure and properties [13]. C_{60} is known to exhibit charge-transfer interaction with electron-donating molecules, such as organic amines, both in the ground and excited states [13]. Here, we discuss charge-transfer interaction of graphene with organic molecules, a property with potential utility in device applications. Raman spectroscopy is eminently effective in probing molecular charge-transfer interactions.

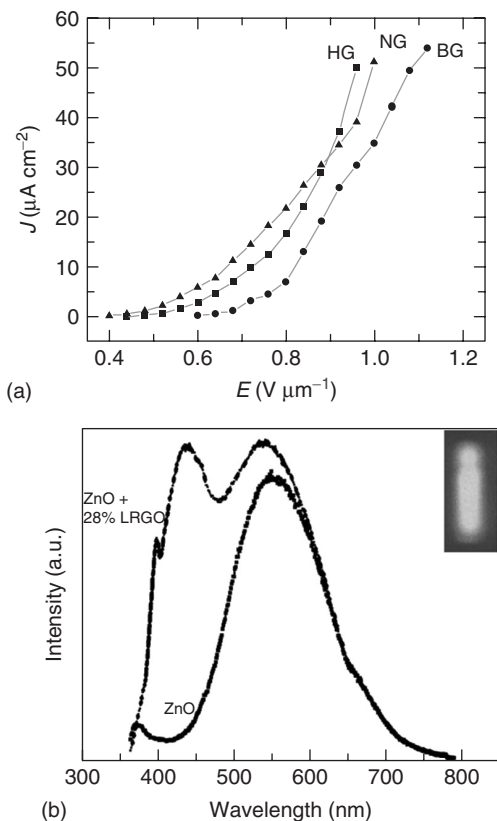


Figure 1.14 (a) Current density (J) of undoped HG, boron-doped BG, and nitrogen-doped NG graphenes as a function of electric field. (Source: Reprinted with permission from Ref. [167].) (b) White-light emission from ZnO-LRGO nanocomposite. (Source: Reprinted with permission from Ref. [168].)

Electron donors such as aniline and TTF soften (i.e., shift to lower frequency) the G-band of FG progressively with the increasing concentration, while electron acceptors such as nitrobenzene and TCNE stiffen (i.e., shift to higher frequency) the G-band, as can be seen in Figure 1.15a,b [12, 13, 172]. Both electron donors and electron acceptors broaden the G-band. The full-width at half maximum (FWHM) of the G-band increases on interaction with these molecules. The intensity of the 2D-band decreases markedly with the concentration of the either donor or acceptor molecule. The ratio of intensities of the 2D- and G-bands, $I_{(2D)}/I_{(G)}$, is a sensitive probe to examine doping of graphene by electron-donor and electron-acceptor molecules. SLGs have also shown similar results. Dong *et al.* [173] have studied the adsorption of various aromatic molecules on SLG films, which cause stiffening or softening of the G-band frequencies because of electronic effects.

Investigations of charge-transfer doping of FG (one layer (1 L) to four layer (4 L)) with Br_2 and I_2 vapors have shown that charge-transfer effects are greater

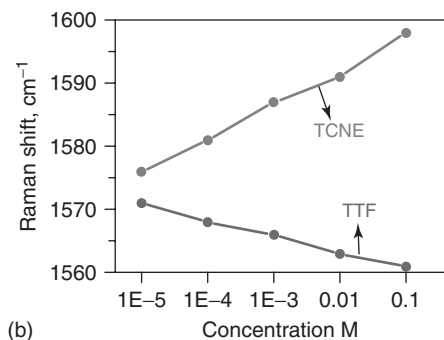
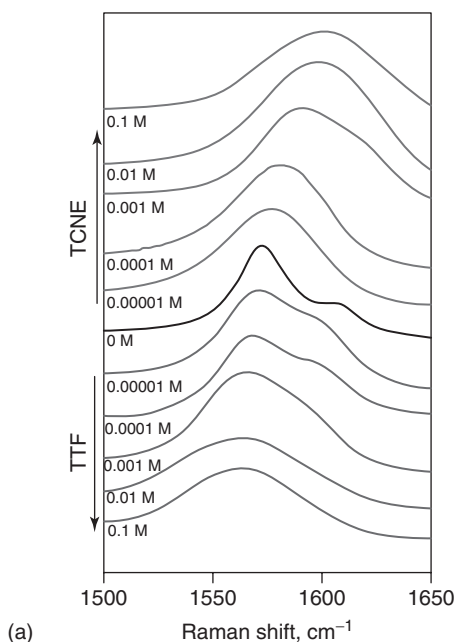


Figure 1.15 (a) Shifts of the Raman G-band of graphene caused by interaction with varying concentrations of TTF and TCNE, and (b) variation in the Raman G-band position of graphene on interaction with varying concentrations of electron-donor (TTF) and electron-acceptor (TCNE) molecules. (Source: Reprinted with permission from Ref. [13].)

on SLGs and bilayer graphenes compared to three- and four-layer graphenes [174]. Detailed studies of the interaction of halogen molecules with graphene have been carried out [175]. Both stiffening of the Raman G-bands on treating with the different halogen molecules and the emergence of new bands in the electronic absorption spectra point to the fact that the halogen molecules are involved in molecular charge transfer with the nanocarbons. The magnitude of molecular charge transfer between the halogens and the nanocarbons generally varies in the order $\text{ICl} > \text{Br}_2 > \text{IBr} > \text{I}_2$ (Figure 1.16), which is consistent with the expected

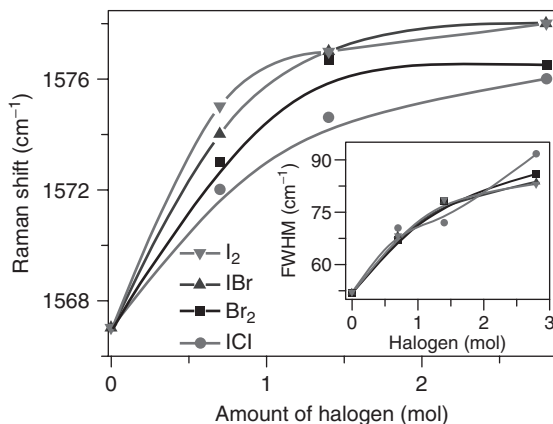


Figure 1.16 G-band characteristics for graphene (inset shows variation in FWHM) for various amounts of different halogens for a fixed molar amount of graphene (1 mol). (Source: Reprinted with permission from Ref. [175].)

order of electron affinities [175]. The occurrence of charge-transfer doping in FG covered with electron-acceptor (TCNE) and electron-donor (TTF) molecules is also evidenced in the electronic absorption spectra and X-ray photoelectron spectroscopy (XPS) [176]. Quantitative estimates of the extent of charge transfer in these complexes have been obtained through XPS. Electrical resistivity of graphene films with and without charge-transfer interactions shows the expected changes [12]. For example, the resistance is lowest in the presence of nitrobenzene and highest in the presence of aniline. There is a systematic dependence of resistance with the electron-donating and electron-withdrawing power of the substituents. The magnitude of interaction between graphene and donor/acceptor molecules seems to depend on the surface area of the graphene sample. Molecular charge transfer affects the magnetic properties of graphene [9]. Magnetization of graphene decreases on adsorption of TTF and TCNE, the interaction with TTF having a greater effect than with TCNE.

Density functional theory (DFT) calculations confirm the occurrence of charge-transfer-induced changes in graphene giving rise to midgap molecular levels with tuning of band gap region near the Dirac point and show how they are different from the effects of electrochemical doping [177, 178]. It has been shown that n-type and p-type graphenes result from charge-transfer interaction of graphene with donor and acceptor molecules, respectively. It is also predicted that the extent of doping depends on the coverage of organic molecules.

1.4.4

Decoration with Metal and Oxide Nanoparticles

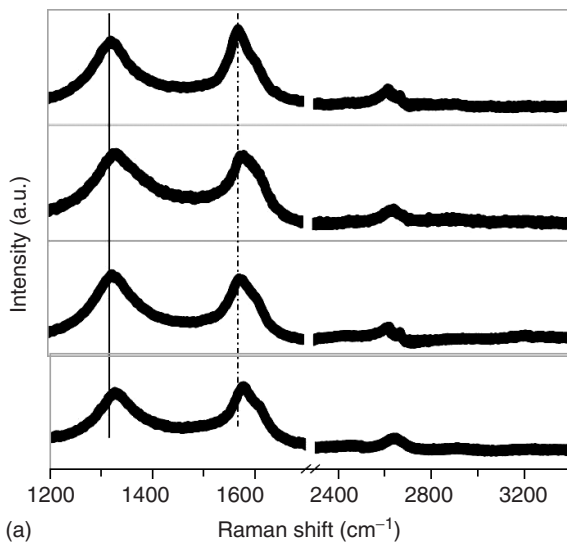
Nanocarbons have been used as support materials for the dispersion and stabilization of metal nanoparticles because of their large chemically active surface and

stability at high temperatures [177]. Decoration with metal nanoparticles results in changing the electronic structure of nanocarbons through Coulombic charge transfer [178]. Combinations of these two materials may lead to a successful integration of their properties in hybrid materials, with possible use in catalysis, nanoelectronics, optics, and nanobiotechnology [179, 180].

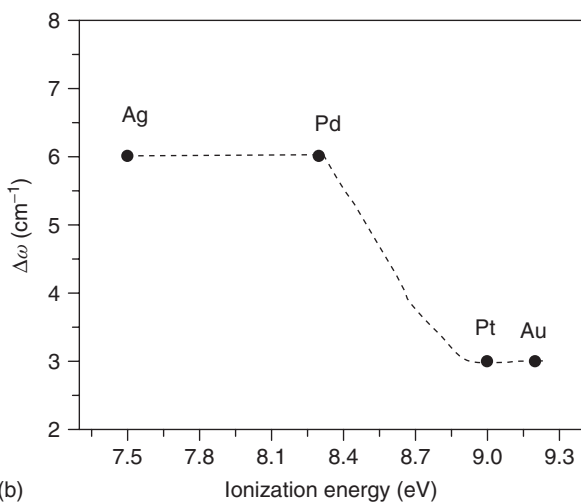
Graphene has been decorated with metal nanoparticles such as Au, Ag, Pt, Pd, and Co by different chemical methods [181]. Decoration of graphene with metal nanoparticles can be followed by absorption spectroscopy and electron microscopy [182]. The influence of metal nanoparticles on the electronic structure of graphene has been examined by Raman spectroscopy and first-principles calculations [183]. There is stiffening in the position of G- and D-bands, and the intensity of the 2D-band relative to that of G-band decreases, whereas the intensity of the D-band relative to that of G-band increases (Figure 1.17a). In comparison with pristine graphene, the FWHM of the G-band shows a significant broadening in graphene-metal composites. The shifts in the G- and D-bands show meaningful trends with the ionization energies of the metals as well as the charge-transfer energies. In Figure 1.17b, we have plotted the frequency shifts of the G-band of EG against the ionization energy (IE) of the metal. Note that the IE varies as $\text{Ag} < \text{Pd} < \text{Pt} < \text{Au}$. Interestingly, the magnitude of the band shifts generally decreases with increase in IE of the metal.

Decoration of graphene with Pt nanoparticles leads to a drastic increase in capacitance value, which is due to high surface area of the composite arresting the aggregation of graphene sheets [184]. Palladium nanoparticle-graphene hybrids are used as efficient catalysts for the Suzuki reaction [185]. Three-dimensional Pt-on-Pd bimetallic nanodendrites supported on graphene nanosheets are used as advanced nanoelectrocatalysts for methanol oxidation [186]. Composites of positively charged gold nanoparticles (GNPs) and pyrene-functionalized graphene (PFG) showed strong electrocatalytic activity and high electrochemical stability [187]. Au films deposited on SLG are used in surface-enhanced Raman scattering (SERS) substrates for the characterization of rhodamine R6G molecules [188]. Silver-decorated graphene oxide (Ag-GO) can be used as an antibacterial material, with a superior antibacterial activity toward *Escherichia coli* [189].

Graphene oxide (GO) is known to interact with nanoparticles of semiconducting oxides such as ZnO and TiO₂ through excited-state electron transfer [181, 190, 191]. The magnetic properties of graphene composites with nanoparticles of ZnO, TiO₂, Fe₃O₄, CoFe₂O₄, and Ni have been studied [192]. Raman studies of the composites of ZnO and TiO₂ with graphene reveal significant shifts in the G-band, with ZnO acting as an electron donor and TiO₂ as an acceptor. These composites also yield higher values of saturation magnetization compared to those of the individual particles or their mechanical mixtures with graphene. Composites of Fe₃O₄ and CoFe₂O₄ with graphene show softening of the G-band revealing a similar charge-transfer interaction, while the saturation magnetization remained without charge. First-principles DFT calculations reveal that the weak charge-transfer interaction and the magnetic coupling are directly linked to the IE and electron affinity of the deposited nanoparticles.



(a)



(b)

Figure 1.17 (a) Raman spectra of EG, EG-Ag, EG-Pt, and EG-Au. (b) Variation in the position of the G-band with the ionization energy of the metal. The broken curve is given as a guide to the eye. (Source: Reprinted with permission from Ref. [183].)

1.4.5

Surface Area and Gas Adsorption

SLG is theoretically predicted to have a large surface area of $2600 \text{ m}^2 \text{ g}^{-1}$ [10], while the surface area of FG is $270\text{--}1550 \text{ m}^2 \text{ g}^{-1}$ [11]. Patchkovskii *et al.* [193] carried out computations considering the contribution of quantum effects to the free energy and the equilibrium constant and suggested that H_2 adsorption capacities

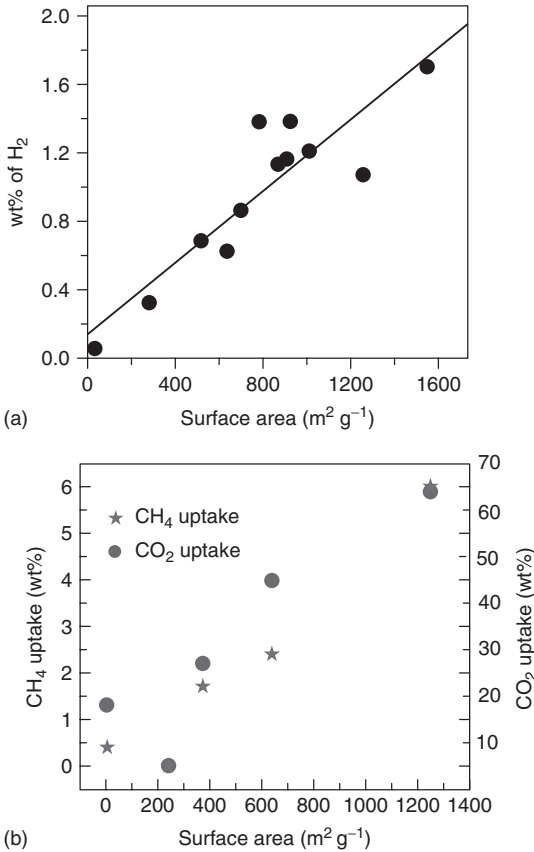


Figure 1.18 (a) Linear relationship between the BET (Brunauer-Emmett-Teller) surface area and weight percentage of hydrogen uptake at 1 atm pressure and 77 K for various graphene samples. (Source: Reprinted with permission from Ref. [194].) (b) Plot of weight percentage of CO₂ uptake (at 195 K and 1 atm) and methane uptake (at 298 K and 5 MPa) versus surface area for different graphene samples. (Source: Reprinted with permission from Ref. [195].)

on graphene can approach values set by the US Department of Energy (DOE) (6.5 wt% and 62 kg of H₂ per cubic meter). H₂ adsorption studies by Ghosh *et al.* [194] on FG samples prepared by the EG and transformation from nanodiamond (ND, DG) have revealed a H₂ uptake value of 1.7 wt% at atmospheric pressure and 77 K. Adsorption of H₂ was found to be directly proportional to the surface area of the samples (Figure 1.18a). A maximum adsorption of 3 wt% was achieved at 298 K and 100 atm for EG.

Uptake of CO₂ and CH₄ by graphenes (EG, HG, RGO, and SGO) was compared with that of activated charcoal [195], and adsorption was found to be dependent on surface areas of the studied samples, with EG showing the highest surface area (640 m² g⁻¹) and SGO showing the lowest (5 m² g⁻¹), while activated charcoal had

a surface area of $1250 \text{ m}^2 \text{ g}^{-1}$. Activated charcoal showed 64 wt% uptake of CO_2 at 195 K and 1 atm, while uptake of CO_2 by EG at 298 K and 50 bar was 51%. The uptake values varied between 5 and 45 wt% in the case of graphene samples at 195 K and 0.1 MPa, with EG exhibiting the highest uptake. EG and RGO samples with relatively high CO_2 uptake capacity contain oxygen functionalities on the surface, while HG with relatively clean surface did not show considerable uptake. However, all the graphenes exhibit smaller uptake capacity for CO_2 compared to activated charcoal, which also has a huge number of surface functional groups. Adsorption of methane on the graphenes and activated charcoal was measured at 273 and 298 K, respectively. The weight uptake of methane by activated charcoal is 7 and 6 wt% at 273 and 298 K and 5 MPa, respectively. The CH_4 uptake of the graphene samples varies between 0 and 3 wt% at 273 K and 5 MPa. Figure 1.18b shows the CO_2 and methane uptake of graphene samples as well as activated charcoal against their surface areas.

1.4.6

Mechanical Properties

Lee *et al.* [7] measured the elastic properties and intrinsic breaking strength of free-standing monolayer graphene membranes by nanoindentation in an AFM. They showed that defect-free monolayer graphene sheets possess excellent mechanical properties such as an elastic modulus of $\sim 1 \text{ TPa}$, a strength of $\sim 130 \text{ GPa}$, and a breaking strength of 42 N m^{-1} . This has led to the exploration of graphene-reinforced polymer matrix composites [196]. Ramanathan *et al.* [197] reported that just $\sim 1 \text{ wt}\%$ addition of graphene to PMMA leads to increases of 80% in elastic modulus and 20% in ultimate tensile strength. A comparative study by these researchers shows that among all the nanofiller materials considered, single-layer functionalized graphene gives the best results (Figure 1.19a). They proposed that nanoscale surface roughness results in an enhanced mechanical interlocking with the polymer chains. Functionalized graphene sheets containing pendant hydroxyl groups across the surfaces may form hydrogen bonds with the carbonyl groups of PMMA and, consequently, stronger interfacial interactions with PMMA. A combined effect of these two enhanced interactions with the polymer matrix is better load transfer between matrix and the fiber resulting in enhancement of mechanical properties. A significant increase of 35 and 45% in the elastic modulus and hardness, respectively, was observed on addition of just 0.6 wt% of graphene to PVA (poly(vinyl alcohol)) [198]. Rafiee *et al.* [199] compared the mechanical properties of epoxy composites of 0.1 wt% of graphene with those of CNTs and found that graphene composites showed much greater increase in Young's modulus (by 31%), tensile strength (by 40%), and fracture toughness (by 53%) than in nanotube-epoxy composites. The fatigue suppression response of nanotube/epoxy composites degrades dramatically as the stress intensity factor amplitude is increased; the reverse effect is seen for graphene-based nanocomposites. Planar geometry of graphene and better matrix adhesion and interlocking arising

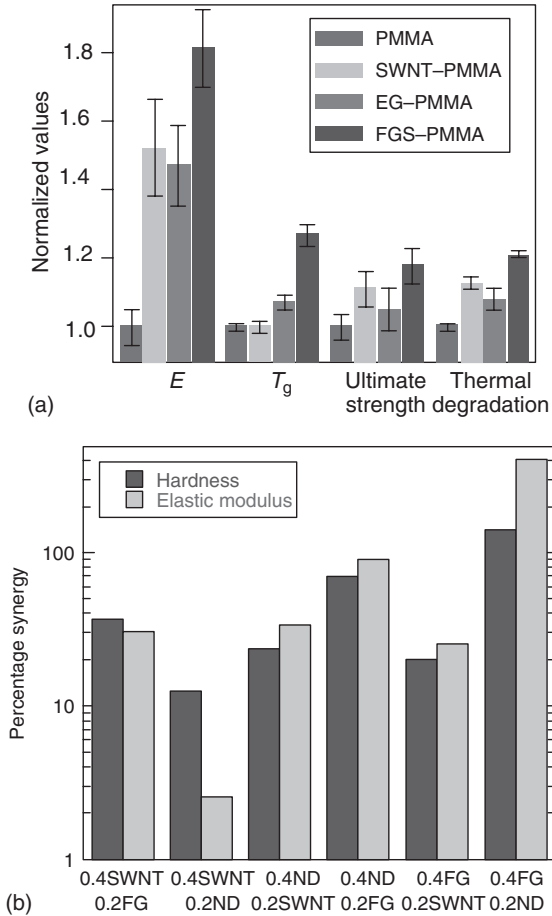


Figure 1.19 (a) Summary of thermomechanical property improvements for 1 wt% single-layer functionalized graphene-PMMA compared to SWNT-PMMA and EG-PMMA composites, with all property values normalized to the values for neat PMMA. (Source:

Reprinted with permission from Ref. [197].)

(b) Percentage synergy in mechanical properties of different binary mixtures of nanodiamond (ND), SWNTs, and few-layered graphene (FG). (Source: Reprinted with permission from Ref. [200].)

from their wrinkled surface is presumed to be the cause of better mechanical properties of graphene composites [199].

Detailed studies of the mechanical properties of binary combinations of ND, FG, and single-walled nanotubes (SWNTs) in PVA matrices have been carried out [200]. The mechanical properties of the resulting composites, evaluated by the nanoindentation technique, showed extraordinary synergy with improvement by as much as 400% in stiffness and hardness compared to those obtained with single nanocarbon reinforcements. The synergistic effect was dramatic in the ND plus FG composites (PVA: 0.4FG-0.2ND) with 4- and 1.5-fold increases in elastic modulus

and hardness, respectively (Figure 1.19b). Variation in the percentage crystallinity (%) of the polymer matrix composite (PMC)s with the two nanocarbons is around 2%, suggesting that increase in crystallinity was not the cause of the observed synergy.

1.4.7

Quenching of Fluorescence of Aromatics

An aspect of graphene chemistry that needs understanding relates to its function in donor–acceptor hybrids with semiconducting organic molecules and polymers. Interaction of electron-donor and electron-acceptor molecules with graphenes has been exploited recently to modify to the electronic properties of graphene through ground-state molecular charge-transfer interactions [12, 13, 201–203]. Fluorescence quenching properties of graphene have been exploited for use in sensitive and selective detection of biomolecules [204]. More recently, the quenching phenomenon has been used for high-contrast visualization of graphene oxide [205] and also in resonance Raman spectroscopy as a substrate to suppress fluorescence [206]. Quenching of the fluorescence of porphyrin by graphene and photophysical properties of porphyrin–graphene complexes has been reported [207, 208]. Theoretical studies show that long-range energy transfer is operative in the fluorescence quenching of a dye molecule in the presence of graphene. The quenching of the green emission of ZnO nanoparticles accompanying the photoreduction of graphene oxide is, however, caused by electron transfer from ZnO. Electron transfer has been similarly invoked in the case of TiO₂/graphene oxide [181].

The interaction of graphene with pyrene-butanoic acid succinimidyl ester, (**PyBS**), **I**, and oligo(*p*-phenylenevinylene) methyl ester (**OPV ester**), **II**, was investigated using a graphene derivative, acid treated thermally exfoliated graphene (EGA), soluble in chloroform and DMF [209]. Absorption spectra of **PyBS**, **I**, in DMF and **OPV ester**, **II**, in chloroform solution (10^{-5} M) are shown in Figure 1.20a,b, respectively, in the presence of varying concentrations of the graphene, EGA. These spectra show characteristic absorption bands of **I** and **II**. The increase in intensities of these bands with the graphene concentration is entirely accounted for the increasing intensity of the graphene absorption band around 270 nm. Thus, electronic absorption spectra of **I** + EGA and **II** + EGA show no evidence of interaction between the two molecules in the ground state. No new absorption bands attributable to charge transfer are also seen. Unlike the absorption spectra, fluorescence spectra of **I** and **II** show remarkable changes on the addition of EGA. The intensity of the fluorescence bands decreases markedly with the increase in EGA concentration, as illustrated in the Figure 1.20c,d. Fluorescence decay measurements on **I** monitored at 395 nm could be fitted to a three-exponential decay [210] with lifetimes of 1.8, 5.7, and 38.7 ns. EGA addition causes a significant decrease in all the three lifetimes, with the values being 1.2, 4.6, and 29.1 ns, respectively, for the addition of 0.3 mg of EGA.

In Figure 1.21a, we compare the transient absorption spectrum of the pure **I** with that of **I** after the addition of 0.3 mg of graphene. The spectrum of **PyBS**

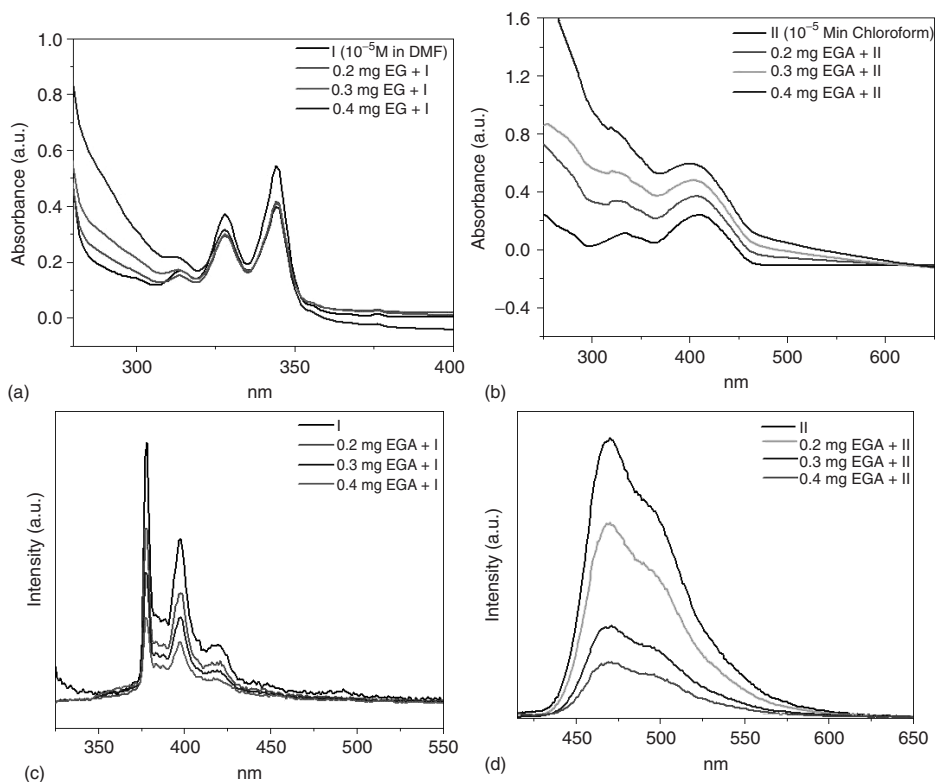


Figure 1.20 Electronic absorption spectra of (a) **PyBS, I**, (10^{-5} M in DMF) and (b) **OPV ester, II**, (10^{-5} M in chloroform), and fluorescence spectra of (c) **PyBS, I**, (10^{-5} M in DMF) and (d) **OPV ester, II**, (10^{-5} M in chloroform) with increasing concentration of graphene (EGA). (Source: Reprinted with permission from Ref. [209].)

shows an absorption maximum around 430 nm together with a broad band in the 450–530 nm range due to the triplet state [211]. On addition of EGA, new bands emerge around 470 and 520 nm in the transient absorption spectrum at 500 ns. The 470 nm band can be assigned to the pyrenyl radical cation as reported in the literature [210], suggesting the occurrence of photo-induced electron transfer from the **PyBS** to the graphene. Accordingly, we observe the transient absorption around 520 nm, which we assign to the graphene radical anion. The decay of the radical cation formed in the presence of graphene was fast, as evidenced from the appearance of a short-lived component (900 ns) in the decay profile (Figure 1.21b). However, the decay of the transient absorption of pure **PyBS** monitored at 470 nm (see inset in Figure 1.21b) shows a long-lived triplet with a lifetime of 6.17 μ s. The transient absorption at 520 nm decays simultaneously with that of the pyrene radical cation indicating that it is due to the graphene radical anion.

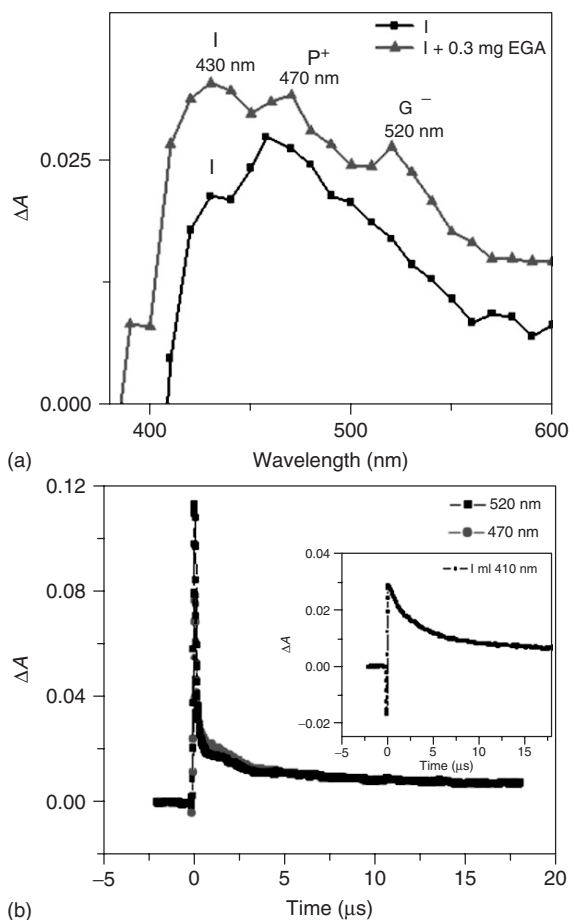


Figure 1.21 (a) Effect of addition of EGA on the transient absorption spectrum of **PyBS**, I, ($\lambda_{\text{exc}} = 355 \text{ nm}$) after 500 ns. (b) Lifetime decay of transient species of **PyBS** + EGA recorded at 470 and 520 nm. Inset shows the decay of pure **PyBS** at 470 nm. (Source: Reprinted with permission from Ref. [209].)

1.4.8

Chemical Storage of Hydrogen and Halogens

Hydrogenation of graphene has been carried out with hydrogen plasma [212–215] and also from molecular H_2 by catalytic hydrogenation [216]. Elias *et al.* [212] reported reversible hydrogenation of graphene films prepared by micromechanical cleavage of graphite. Hydrogenation was obtained with cold hydrogen plasma containing hydrogen–argon mixture (10% H_2). The hydrogenated sample showed electronic behavior quite different from that of graphene, with evidence of metallic to insulator transition. The original properties of graphene were regained on heating the hydrogenated sample at 450°C for 24 h. Catalytic hydrogenation of

graphene using the radio frequency catalytic chemical vapor deposition (rf-cCVD) method was adopted by Zheng *et al.* [216] Ni (8 wt%) in Al₂O₃ was used as catalyst. Hydrogenation was confirmed by the appearance of peaks at 2920 and 2853 cm⁻¹ in (C–H stretching modes) in IR spectra and increase in intensity of D-band in the Raman spectrum of hydrogenated samples. They also observed that on hydrogenation, samples turned hydrophobic, while the original graphene sample was hydrophilic. We have carried out plasma hydrogenation of graphene samples prepared by arc discharge in H₂ (HG). Elemental analysis of samples for two different plasma conditions (100 W, 20 min), one at room temperature and other at 170 °C, showed the presence of ~1.25 and 1.78 wt% of hydrogen, respectively. On plasma hydrogenation, the intensity of the D-band in the Raman spectrum increased with respect to the G-band, while that of the 2D-band decreased. Increased defect in graphene lattice caused origin of new band at 2909 cm⁻¹(D + G). Chemical hydrogenation of various graphene samples (EG and HG) by the Birch reduction has been performed [123]. Evidence of hydrogenation were obtained from appearance of C–H stretching modes in the IR spectra of hydrogenated samples, as can be seen from Figure 1.22a. An increase in the intensity of D-band relative to G-band in the Raman spectrum of hydrogenated exfoliation of graphite (EGH) and hydrogenated HG (HGH) samples reflects an increase in the sp³ character. The UV spectrum of graphene is also affected on reduction, wherein the intensity of the 260 nm band decreases progressively, with a new band appearing around 235 nm. Magnetization of the graphene samples increases on hydrogenation. Elemental analysis of reduced graphene samples showed the hydrogen content to be around 5 wt%. Thermal analysis of EGH and HGH showed that these samples were stable at room temperature for prolonged period. Heating initiates the H₂ loss, as can be seen from Figure 1.22b. Almost all the H₂ was lost by 500 °C and the sample regained its original properties. Dehydrogenation could also be obtained by irradiation of the hydrogenated samples with UV rays or with a KrF excimer laser. On dehydrogenation, the sample regains all its properties and becomes graphene-like. The Birch reduction of GNRs prepared by oxidative unzipping of CNTs showed H₂ uptake of 3 wt%. Thermal analysis of the sample showed H₂ loss initiating at 300 °C and completing by 600 °C, with the release of 3.05 wt% H₂ during this period. Maximum H₂ loss occurs at 400 °C. The sample starts degrading at temperatures beyond 550 °C, which might be due to the presence of some functional groups from the initial oxidation treatment used to unzip the nanotubes.

We have examined the UV irradiation of graphene (HG and EG) in liquid chlorine medium resulting in graphene chlorination of 56 wt% [217]. The core level X-ray photoelectron spectrum of the product showed three features centered at 284.6, 285.8, and 287.6 eV corresponding to sp²- and sp³-hybridized carbons and C–Cl, respectively, as shown in Figure 1.22. The composition of the sample as determined by the ratio of the intensity of Cl 2p to that of the C 1s peak (taking into account the atomic sensitivity factors of Cl 2p and C 1s) was 30 at% of chlorine (~56 wt%). Interestingly, chlorination too was reversible. A temperature-dependent stability study of the chlorinated sample showed that the sample was stable at room

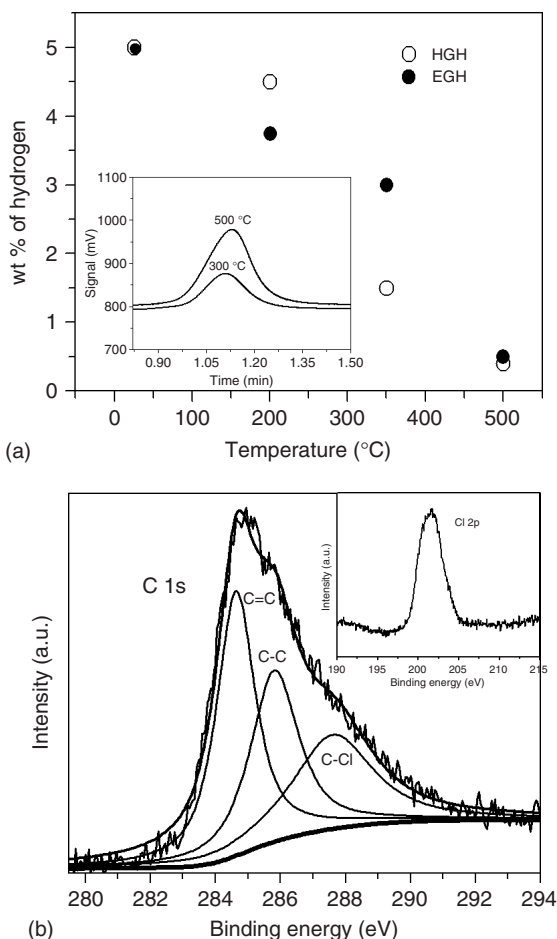


Figure 1.22 (a) Change in weight percentage of hydrogen released from EGH and HGH with temperature. In inset is shown the evolution of hydrogen as recorded by gas chromatography. (Source: Reprinted

with permission from Ref. [123].) (b) C 1s core level XP spectrum of photo-chlorinated graphene. Inset shows the Cl 2p signal in XPS. (Source: Reprinted with permission from Ref. [217].)

temperature for long periods, but slowly lost Cl_2 on progressive heating, with complete loss of Cl_2 by 500°C . IR spectra of samples taken at various stages of heating showed progressive decrease in the intensity of the C-Cl band at 790 cm^{-1} . We could also eliminate all the chlorine on irradiation with a laser (Lambda Physik KrF excimer laser ($\lambda = 248\text{ nm}$, $\tau = 30\text{ ns}$, rep. rate = 5 Hz , laser energy = 370 mJ)). Dechlorination appears to be associated with a small barrier just as the decomposition of hydrogenated graphene. The strain in the chlorinated sample appears to drive the dechlorination to form the more stable

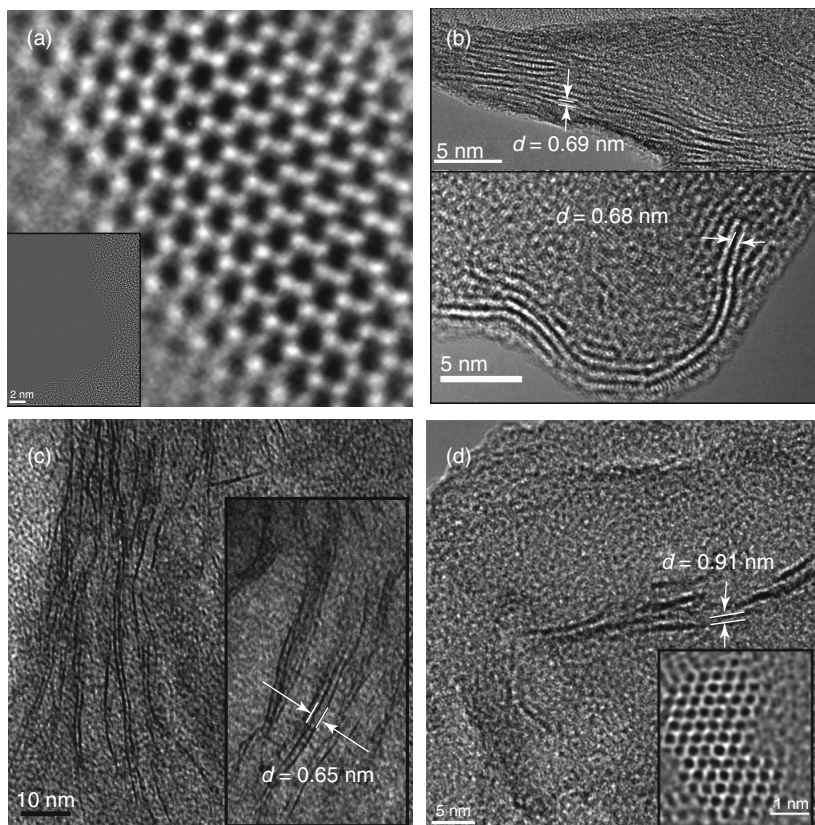


Figure 1.23 TEM images of MoS₂ layers obtained by (a) heating molybdic acid with an excess of thiourea at 773 K, (b) hydrothermal reaction between MoO₃ and KSCN, (c) high-resolution TEM image of layered MoS₂ from hydrothermal conditions, and

(d) images of WS₂ layers obtained from Li intercalation and exfoliation of bulk WS₂ and heating molybdic acid with an excess of thiourea at 773 K, respectively. The bends in the layers may arise from defects. (Source: Reprinted with permission from Ref. [218].)

graphene. Bromination of graphene up to 25 wt% is achieved, and the bromine is fully eliminated by 500 °C. The study demonstrates that FG can be used to store chlorine and bromine.

1.5

Inorganic Graphene Analogs

There are many inorganic compounds with layered structures, the most well known being MoS₂, WS₂, and BN. Fullerene-type structures of these materials were made some years ago, soon followed by nanotube structures of these materials. It is, therefore, not surprising that one should be able to make graphene

analogs of such layered materials. During the past year, graphene-like structures of MoS₂, WS₂, MoSe₂, WSe₂, BN, and other materials have indeed been prepared and characterized. The layered structures of MoS₂, WS₂, MoSe₂, and WSe₂ with different numbers of layers have been made by chemical methods and also by sonication in polar solvents [218–223]. The chemical methods include Li intercalation and exfoliation, hydrothermal synthesis, and reaction of molybdic and tungstic acids with excess of thiourea or selenourea in a N₂ atmosphere at 773 K [218, 223]. Figure 1.23a,b show graphene-like MoS₂ layers obtained by reaction of molybdic acid with thiourea and hydrothermal synthesis, respectively, with a layer separation in the range of 0.65–0.7 nm. The high-resolution image in Figure 1.23c shows the hexagonal structure formed by Mo and S atoms with a Mo–S distance of 2.30 Å. BN with different numbers of layers has also been made by chemical methods involving reaction of boric acid and urea at high temperatures [224]. WS₂ obtained by both hydrothermal and intercalation methods mostly consist of bilayers and single layers, as can be seen in the TEM images in Figure 1.23d,e. The spacing between the WS₂ layers in the bilayer sample is in the range of 0.65–0.70 nm. WS₂ layers obtained by the thiourea method show an interlayer spacing of 0.9 nm. BCN is another graphene analog obtained by the reaction of high-surface-area activated charcoal with a mixture of boric acid and urea or by vapor-phase synthesis from a mixture of BBr₃, ethylene, and ammonia [225, 226]. Besides their structural features, some of the properties of inorganic graphene analogs have been studied. For example, transistors have been made out of one- or few-layer MoS₂ and MoSe₂ [227]. Mechanical properties of polymer composites containing different number of layers of BN have been studied [228]. Greater improvement in mechanical properties is found to occur when BN with a fewer number of layers is imported into the composites. Clearly, several new graphene-like inorganic materials will be prepared in the next few years, and many of them may indeed possess interesting and useful properties.

References

1. Novoselov, K.S., Geim, A.K., Morozov, S.V., Jiang, D., Zhang, Y., Dubonos, S.V., Grigorieva, I.V., and Firsov, A.A. (2004) *Science*, **306**, 666.
2. Novoselov, K.S., Geim, A.K., Morozov, S.V., Jiang, D., Katsnelson, M.I., Grigorieva, I.V., Dubonos, S.V., and Firsov, A.A. (2005) *Nature*, **438**, 197.
3. Rao, C.N.R., Sood, A.K., Subrahmanyam, K.S., and Govindaraj, A. (2009) *Angew. Chem. Int. Ed.*, **48**, 7752.
4. Chen, J.-H., Jang, C., Xiao, S., Ishigami, M., and Fuhrer, M.S. (2008) *Nat. Nanotechnol.*, **3**, 206.
5. Han, M.Y., Oezylmaz, B., Zhang, Y., and Kim, P. (2007) *Phys. Rev. Lett.*, **98**, 206805.
6. Nair, R.R., Blake, P., Grigorenko, A.N., Novoselov, K.S., Booth, T.J., Stauber, T., Peres, N.M.R., and Geim, A.K. (2008) *Science*, **320**, 1308.
7. Lee, C., Wei, X., Kysar, J.W., and Hone, J. (2008) *Science*, **321**, 385.
8. Wang, Y., Huang, Y., Song, Y., Zhang, X.Y., Ma, Y.F., Liang, J.J., and Chen, Y.S. (2009) *Nano Lett.*, **9**, 220.

9. Matte, H.S.S.R., Subrahmanyam, K.S., and Rao, C.N.R. (2009) *J. Phys. Chem. C*, **113**, 9982.
10. Peigney, A., Laurent, C., Flahaut, E., Bacsá, R.R., and Rousset, A. (2001) *Carbon*, **39**, 507.
11. Rao, C.N.R., Sood, A.K., Voggu, R., and Subrahmanyam, K.S. (2010) *J. Phys. Chem. Lett.*, **1**, 572.
12. Das, B., Voggu, R., Rout, C.S., and Rao, C.N.R. (2008) *Chem. Commun.*, 5155.
13. Rao, C.N.R. and Voggu, R. (2010) *Mater. Today*, **13**, 34.
14. Abergel, D.S.L., Russell, A., and Falko, V.I. (2007) *Appl. Phys. Lett.*, **91**, 063125.
15. Ni, Z.H., Wang, H.M., Kasim, J., Fan, H.M., Yu, T., Wu, Y.H., Feng, Y.P., and Shen, Z.X. (2007) *Nano Lett.*, **7**, 2758.
16. Gao, L., Ren, W., Li, F., and Cheng, H.-M. (2008) *ACS Nano*, **2**, 1625.
17. Hiura, H., Miyazaki, H., and Tsukagoshi, K. (2010) *Appl. Phys. Exp.*, **3**, 095101.
18. Kochat, V., Nath Pal, A., Sneha, E.S., Sampathkumar, A., Gairola, A., Shivashankar, S.A., Raghavan, S., and Ghosh, A. (2011) *J. Appl. Phys.*, **110**, 014315.
19. Gass, M.H., Bangert, U., Bleloch, A.L., Wang, P., Nair, R.R., and Geim, A.K. (2008) *Nat. Nanotechnol.*, **3**, 676.
20. Meyer, J.C., Kisielowski, C., Erni, R., Rossell, M.D., Crommie, M.F., and Zettl, A. (2008) *Nano Lett.*, **8**, 3582.
21. Wu, Y.H., Yu, T., and Shen, Z.X. (2010) *J. Appl. Phys.*, **108**, 071301.
22. Hernandez, Y., Nicolosi, V., Lotya, M., Blighe, F.M., Sun, Z., De, S., McGovern, I.T., Holland, B., Byrne, M., Gun'Ko, Y.K., Boland, J.J., Niraj, P., Duesberg, G., Krishnamurthy, S., Goodhue, R., Hutchison, J., Scardaci, V., Ferrari, A.C., and Coleman, J.N. (2008) *Nat. Nanotechnol.*, **3**, 563.
23. Geim, A.K. and Novoselov, K.S. (2007) *Nat. Mater.*, **6**, 183.
24. Hiura, H., Ebbesen, T.W., Fujita, J., Tanigaki, K., and Takada, T. (1994) *Nature*, **367**, 148.
25. Ebbesen, T.W. and Hiura, H. (1995) *Adv. Mater.*, **7**, 582.
26. Bernhardt, T.M., Kaiser, B., and Rademann, K. (1998) *Surf. Sci.*, **408**, 86.
27. Roy, H. (1998) *J. Appl. Phys.*, **83**, 4695.
28. Lu, X., Yu, M., Huang, H., and Ruoff, R.S. (1999) *Nanotechnology*, **10**, 269.
29. Roy, H.V., Kallinger, C., and Sattler, K. (1998) *Surf. Sci.*, **407**, 1.
30. Zhang, Y. (2005) *Appl. Phys. Lett.*, **86**, 073104.
31. Marcano, D.C., Kosynkin, D.V., Berlin, J.M., Sinititskii, A., Sun, Z., Slesarev, A., Alemany, L.B., Lu, W., and Tour, J.M. (2010) *ACS Nano*, **4**, 4806.
32. Park, S., An, J., Jung, I., Piner, R.D., An, S.J., Li, X., Velamakanni, A., and Ruoff, R.S. (2009) *Nano Lett.*, **9**, 1593.
33. Hummers, W.S. and Offeman, R.E. (1958) *J. Am. Chem. Soc.*, **80**, 1339.
34. Allen, M.J., Tung, V.C., and Kaner, R.B. (2009) *Chem. Rev.*, **110**, 132.
35. Tung, V.C., Allen, M.J., Yang, Y., and Kaner, R.B. (2009) *Nat. Nanotechnol.*, **4**, 25.
36. Paredes, J.I., Villar-Rodil, S., Marti'nez-Alonso, A., and Tasco'n, J.M.D. (2008) *Langmuir*, **24**, 10560.
37. Schniepp, H.C., Li, J.-L., McAllister, M.J., Sai, H., Herrera-Alonso, M., Adamson, D.H., Prud'homme, R.K., Car, R., Saville, D.A., and Aksay, I.A. (2006) *J. Phys. Chem. B*, **110**, 8535.
38. McAllister, M.J., Li, J.-L., Adamson, D.H., Schniepp, H.C., Abdala, A.A., Liu, J., Herrera-Alonso, M., Milius, D.L., Car, R., Prud'homme, R.K., and Aksay, I.A. (2007) *Chem. Mater.*, **19**, 4396.
39. Li, X., Zhang, G., Bai, X., Sun, X., Wang, X., Wang, E., and Dai, H. (2008) *Nat. Nanotechnol.*, **3**, 538.
40. Guoqing, X., Wontae, H., Namhun, K., Sung, M.C., and Heeyeop, C. (2010) *Nanotechnology*, **21**, 405201.
41. Liang, X., Chang, A.S.P., Zhang, Y., Harteneck, B.D., Choo, H., Olynick, D.L., and Cabrini, S. (2008) *Nano Lett.*, **9**, 467.
42. Qian, M. (2011) *Appl. Phys. Lett.*, **98**, 173108.

43. Viculis, L.M., Mack, J.J., Mayer, O.M., Hahn, H.T., and Kaner, R.B. (2005) *J. Mater. Chem.*, **15**, 974.
44. Valles, C., Drummond, C., Saadaoui, H., Furtado, C.A., He, M., Roubeau, O., Ortolani, L., Monthieux, M., and Pénicaud, A. (2008) *J. Am. Chem. Soc.*, **130**, 15802.
45. Ghosh, A., Rao, K.V., George, S.J., and Rao, C.N.R. (2010) *Chem. Eur. J.*, **16**, 2700.
46. Bourlinos, A.B., Georgakilas, V., Zboril, R., Steriotis, T.A., and Stubos, A.K. (2009) *Small*, **5**, 1841.
47. Hamilton, C.E., Lomeda, J.R., Sun, Z., Tour, J.M., and Barron, A.R. (2009) *Nano Lett.*, **9**, 3460.
48. O'Neill, A., Khan, U., Nirmalraj, P.N., Boland, J., and Coleman, J.N. (2011) *J. Phys. Chem. C*, **115**, 5422.
49. Hernandez, Y., Lotya, M., Rickard, D., Bergin, S.D., and Coleman, J.N. (2009) *Langmuir*, **26**, 3208.
50. Wang, X., Fulvio, P.F., Baker, G.A., Veith, G.M., Unocic, R.R., Mahurin, S.M., Chi, M., and Dai, S. (2010) *Chem. Commun.*, **46**, 4487.
51. Choucair, M., Thordarson, P., and Stride, J.A. (2009) *Nat. Nanotechnol.*, **4**, 30.
52. Kim, K.S., Zhao, Y., Jang, H., Lee, S.Y., Kim, J.M., Kim, K.S., Ahn, J.-H., Kim, P., Choi, J.-Y., and Hong, B.H. (2009) *Nature*, **457**, 706.
53. Kwon, S.-Y., Ciobanu, C.V., Petrova, V., Shenoy, V.B., Barenó, J., Gambin, V., Petrov, I., and Kodambaka, S. (2009) *Nano Lett.*, **9**, 3985.
54. Sutter, P.W., Flege, J.-I., and Sutter, E.A. (2008) *Nat. Mater.*, **7**, 406.
55. Coraux, J., N'Diaye, A.T., Busse, C., and Michely, T. (2008) *Nano Lett.*, **8**, 565.
56. Li, X., Cai, W., An, J., Kim, S., Nah, J., Yang, D., Piner, R., Velamakanni, A., Jung, I., Tutuc, E., Banerjee, S.K., Colombo, L., and Ruoff, R.S. (2009) *Science*, **324**, 1312.
57. Reina, A., Jia, X., Ho, J., Nezich, D., Son, H., Bulovic, V., Dresselhaus, M.S., and Kong, J. (2008) *Nano Lett.*, **9**, 30.
58. Wang, J.J., Zhu, M.Y., Outlaw, R.A., Zhao, X., Manos, D.M., Holloway, B.C., and Mammanna, V.P. (2004) *Appl. Phys. Lett.*, **85**, 1265.
59. Wang, J., Zhu, M., Outlaw, R.A., Zhao, X., Manos, D.M., and Holloway, B.C. (2004) *Carbon*, **42**, 2867.
60. Zhu, M., Wang, J., Holloway, B.C., Outlaw, R.A., Zhao, X., Hou, K., Shutthanandan, V., and Manos, D.M. (2007) *Carbon*, **45**, 2229.
61. Rao, C.N.R., Subrahmanyam, K.S., Ramakrishna Matte, H.S.S., Abdulhakeem, B., Govindaraj, A., Das, B., Kumar, P., Ghosh, A., and Late, D.J. (2010) *Sci. Technol. Adv. Mater.*, **11**, 054502.
62. Pati, S.K., Enoki, T., and Rao, C.N.R. (2010) *Graphene and its Fascinating Attributes*, World Scientific Publishing Co., Chennai.
63. Subrahmanyam, K.S., Panchakarla, L.S., Govindaraj, A., and Rao, C.N.R. (2009) *J. Phys. Chem. C*, **113**, 4257.
64. Panchakarla, L.S., Govindaraj, A., and Rao, C.N.R. (2009) *Inorg. Chim. Acta*, **363**, 4163.
65. Wu, Z.-S., Ren, W., Gao, L., Zhao, J., Chen, Z., Liu, B., Tang, D., Yu, B., Jiang, C., and Cheng, H.-M. (2009) *ACS Nano*, **3**, 411.
66. Zhiyong, W., Nan, L., Zujin, S., and Zhennan, G. (2010) *Nanotechnology*, **21**, 175602.
67. Li, N., Wang, Z., Zhao, K., Shi, Z., Gu, Z., and Xu, S. (2010) *Carbon*, **48**, 255.
68. Wu, C., Dong, G., and Guan, L. (2010) *Phys. E*, **42**, 1267.
69. Dreyer, D.R., Park, S., Bielawski, C.W., and Ruoff, R.S. (2010) *Chem. Soc. Rev.*, **39**, 228.
70. Stankovich, S., Dikin, D.A., Piner, R.D., Kohlhaas, K.A., Kleinhammes, A., Jia, Y., Wu, Y., Nguyen, S.T., and Ruoff, R.S. (2007) *Carbon*, **45**, 1558.
71. Shin, H.-J., Kim, K.K., Benayad, A., Yoon, S.-M., Park, H.K., Jung, I.-S., Jin, M.H., Jeong, H.-K., Kim, J.M., Choi, J.-Y., and Lee, Y.H. (2009) *Adv. Funct. Mater.*, **19**, 1987.
72. Pham, V.H., Cuong, T.V., Nguyen-Phan, T.-D., Pham, H.D., Kim, E.J., Hur, S.H., Shin, E.W., Kim, S., and Chung, J.S. (2010) *Chem. Commun.*, **46**, 4375.

73. Zhou, X., Zhang, J., Wu, H., Yang, H., Zhang, J., and Guo, S. (2011) *J. Phys. Chem. C*, **115**, 11957.
74. Zhu, C., Guo, S., Fang, Y., and Dong, S. (2010) *ACS Nano*, **4**, 2429.
75. Zhang, J., Yang, H., Shen, G., Cheng, P., Zhang, J., and Guo, S. (2010) *Chem. Commun.*, **46**, 1112.
76. Wang, G., Yang, J., Park, J., Gou, X., Wang, B., Liu, H., and Yao, J. (2008) *J. Phys. Chem.*, **112**, 8192.
77. Fan, X., Peng, W., Li, Y., Li, X., Wang, S., Zhang, G., and Zhang, F. (2008) *Adv. Mater.*, **20**, 4490.
78. Amarnath, C.A., Hong, C.E., Kim, N.H., Ku, B.-C., Kuila, T., and Lee, J.H. (2011) *Carbon*, **49**, 3497.
79. Guo, H.-L., Wang, X.-F., Qian, Q.-Y., Wang, F.-B., and Xia, X.-H. (2009) *ACS Nano*, **3**, 2653.
80. Sundaram, R.S., Gómez-Navarro, C., Balasubramanian, K., Burghard, M., and Kern, K. (2008) *Adv. Mater.*, **20**, 3050.
81. Compton, O.C., Jain, B., Dikin, D.A., Abouimrane, A., Amine, K., and Nguyen, S.T. (2011) *ACS Nano*, **5**, 4380.
82. Zhou, M., Wang, Y., Zhai, Y., Zhai, J., Ren, W., Wang, F., and Dong, S. (2009) *Chem. Eur. J.*, **15**, 6116.
83. Ding, Y.H. *et al.* (2011) *Nanotechnology*, **22**, 215601.
84. Cote, L.J., Cruz-Silva, R., and Huang, J. (2009) *J. Am. Chem. Soc.*, **131**, 11027.
85. Abdelsayed, V., Moussa, S., Hassan, H.M., Aluri, H.S., Collinson, M.M., and El-Shall, M.S. (2010) *J. Phys. Chem. Lett.*, **1**, 2804.
86. Kumar, P., Das, B., Chitara, B., Subrahmanyam, K.S., Gopalakrishnan, K., Krupanidhi, S.B., and Rao, C.N.R. (2012) *Macromol. Chem. Phys.*, **213**, 1146.
87. Kumar, P., Subrahmanyam, K.S., and Rao, C.N.R. (2011) *Mater. Exp.*, **1**, 252.
88. Baraket, M., Walton, S.G., Wei, Z., Lock, E.H., Robinson, J.T., and Sheehan, P. (2010) *Carbon*, **48**, 3382.
89. Ekiz, O.O., Urel, M., Guner, H., Mizrak, A.K., and Dana, A. (2011) *ACS Nano*, **5**, 2475.
90. Yao, P., Chen, P., Jiang, L., Zhao, H., Zhu, H., Zhou, D., Hu, W., Han, B.-H., and Liu, M. (2010) *Adv. Mater.*, **22**, 5008.
91. Hassan, H.M.A., Abdelsayed, V., Khder, A.E.R.S., AbouZeid, K.M., Terner, J., El-Shall, M.S., Al-Resayes, S.I., and El-Azhary, A.A. (2009) *J. Mater. Chem.*, **19**, 3832.
92. Li, Z., Yao, Y., Lin, Z., Moon, K.-S., Lin, W., and Wong, C. (2010) *J. Mater. Chem.*, **20**, 4781.
93. Li, X., Wang, X., Zhang, L., Lee, S., and Dai, H. (2008) *Science*, **319**, 1229.
94. Wang, X., Ouyang, Y., Li, X., Wang, H., Guo, J., and Dai, H. (2008) *Phys. Rev. Lett.*, **100**, 206803.
95. Cresti, A., Nemeč, N., Biel, B., Niebler, G., Triozon, Fo., Cuniberti, G., and Roche, S. (2008) *Nano Res.*, **1**, 361.
96. Chen, Z., Lin, Y.-M., Rooks, M.J., and Avouris, P. (2007) *Phys. E*, **40**, 228.
97. Tapasztó, L., Dobrik, G., Lambin, P., and Biro, L.P. (2008) *Nat. Nanotechnol.*, **3**, 397.
98. Cano-Marquez, A.G., Rodríguez-Macias, F.J., Campos-Delgado, J., Espinosa-Gonzalez, C.G., Tristan-Lopez, F., Ramirez-Gonzalez, D., Cullen, D.A., Smith, D.J., Terrones, M., and Vega-Cantu, Y.I. (2009) *Nano Lett.*, **9**, 1527.
99. Kosynkin, D.V., Higginbotham, A.L., Sinitskii, A., Lomeda, J.R., Dimiev, A., Price, B.K., and Tour, J.M. (2009) *Nature*, **458**, 872.
100. Higginbotham, A.L., Kosynkin, D.V., Sinitskii, A., Sun, Z., and Tour, J.M. (2010) *ACS Nano*, **4**, 2059.
101. Jiao, L., Wang, X., Diankov, G., Wang, H., and Dai, H. (2011) *Nat. Nanotechnol.*, **6**, 132.
102. Kosynkin, D.V., Lu, W., Sinitskii, A., Pera, G., Sun, Z., and Tour, J.M. (2011) *ACS Nano*, **5**, 968.
103. Jiao, L., Zhang, L., Wang, X., Diankov, G., and Dai, H. (2009) *Nature*, **458**, 877.
104. Wu, Z.-S., Ren, W., Gao, L., Liu, B., Zhao, J., and Cheng, H.-M. (2010) *Nano Res.*, **3**, 16.
105. Kumar, P., Panchakarla, L.S., and Rao, C.N.R. (2011) *Nanoscale*, **3**, 2127.
106. Yu, W.J., Chae, S.H., Perello, D., Lee, S.Y., Han, G.H., Yun, M., and Lee, Y.H. (2010) *ACS Nano*, **4**, 5480.

107. Wang, X. and Dai, H. (2010) *Nat. Chem.*, **2**, 661.
108. Cai, J., Ruffieux, P., Jaafar, R., Bieri, M., Braun, T., Blankenburg, S., Muoth, M., Seitsonen, A.P., Saleh, M., Feng, X., Mullen, K., and Fasel, R. (2010) *Nature*, **466**, 470.
109. Yang, X., Dou, X., Rouhanipour, A., Zhi, L., Rader, H.J., and Mullen, K. (2008) *J. Am. Chem. Soc.*, **130**, 4216.
110. Yazyev, O.V. and Helm, L. (2007) *Phys. Rev. B*, **75**, 125408.
111. Bhowmick, S. and Shenoy, V.B. (2008) *J. Chem. Phys.*, **128**, 244717.
112. Joly, V.L.J., Takahara, K., Takai, K., Sugihara, K., Enoki, T., Koshino, M., and Tanaka, H. (2010) *Phys. Rev. B*, **81**, 115408.
113. Kopelevich, Y., da Silva, R.R., Torres, J.H.S., Penicaud, A., and Kyotani, T. (2003) *Phys. Rev. B*, **68**, 092408.
114. Talapatra, S., Ganesan, P.G., Kim, T., Vajtai, R., Huang, M., Shima, M., Ramanath, G., Srivastava, D., Deevi, S.C., and Ajayan, P.M. (2005) *Phys. Rev. Lett.*, **95**, 097201.
115. Shenoy, V.B. and Rao, C.N.R. (2008) *Philos. Trans. R. Soc. A*, **366**, 63.
116. Shenoy, V.B., Sarma, D.D., and Rao, C.N.R. (2006) *Chem. Phys. Chem.*, **7**, 2053.
117. Dutta, S., Lakshmi, S., and Pati, S.K. (2008) *Phys. Rev. B*, **77**, 073412.
118. Sato, H., Kawatsu, N., Enoki, T., Endo, M., Kobori, R., Maruyama, S., and Kaneko, K. (2003) *Solid State Commun.*, **125**, 641.
119. Hao, S., Takai, K., Feiyu, K., and Enoki, T. (2008) *Carbon*, **46**, 110.
120. Takai, K., Eto, S., Inaguma, M., Enoki, T., Ogata, H., Tokita, M., and Watanabe, J. (2007) *Phys. Rev. Lett.*, **98**, 017203.
121. Enoki, T. and Takai, K. (2008) *Dalton Trans.*, 3773.
122. Makarova, T. and Palacio, F. (2006) *Carbon Based Magnetism*, Elsevier, Amsterdam.
123. Subrahmanyam, K.S., Kumar, P., Maitra, U., Govindaraj, A., Hembram, K., Waghmare, U.V., and Rao, C.N.R. (2011) *Proc. Natl. Acad. Sci. U.S.A.*, **108**, 2674.
124. Late, D.J., Ghosh, A., Subrahmanyam, K.S., Panchakarla, L.S., Krupanidhi, S.B., and Rao, C.N.R. (2010) *Solid State Commun.*, **150**, 734.
125. Vasko, F.T. and Ryzhii, V. (2007) *Phys. Rev. B*, **76**, 233404.
126. Hwang, E.H. and Das Sarma, S. (2008) *Phys. Rev. B*, **77**, 115449.
127. Stauber, T., Peres, N.M.R., and Guinea, F. (2007) *Phys. Rev. B*, **76**, 205423.
128. Hwang, E.H., Adam, S., and Das Sarma, S. (2007) *Phys. Rev. Lett.*, **98**, 186806.
129. Chen, J.H., Jang, C., Adam, S., Fuhrer, M.S., Williams, E.D., and Ishigami, M. (2008) *Nat. Phys.*, **4**, 377.
130. Morozov, S.V., Novoselov, K.S., Katsnelson, M.I., Schedin, F., Elias, D.C., Jaszczak, J.A., and Geim, A.K. (2008) *Phys. Rev. Lett.*, **100**, 016602.
131. Du, X., Skachko, I., Barker, A., and Andrei, E.Y. (2008) *Nat. Nanotechnol.*, **3**, 491.
132. Schwierz, F. (2010) *Nat. Nanotechnol.*, **5**, 487.
133. Vollmer, A., Feng, X., Wang, X., Zhi, L., Mullen, K., Koch, N., and Rabe, J. (2009) *Appl. Phys. A*, **94**, 1.
134. Mak, K.F., Sfeir, M.Y., Wu, Y., Lui, C.H., Misewich, J.A., and Heinz, T.F. (2008) *Phys. Rev. Lett.*, **101**, 196405.
135. Kim, W.Y. and Kim, K.S. (2008) *Nat. Nanotechnol.*, **3**, 408.
136. Bai, J.W., Cheng, R., Xiu, F.X., Liao, L., Wang, M.S., Shailos, A., Wang, K.L., Huang, Y., and Duan, X.F. (2010) *Nat. Nanotechnol.*, **5**, 655.
137. Bai, J., Duan, X., and Huang, Y. (2009) *Nano Lett.*, **9**, 2083.
138. Heersche, H.B., Jarillo-Herrero, P., Oostinga, J.B., Vandersypen, L.M.K., and Morpurgo, A.F. (2007) *Nature*, **446**, 56.
139. Qifeng, L. and Jinming, D. (2008) *Nanotechnology*, **19**, 355706.
140. Masatsugu, S., Itsuko, S.S., and Jurgen, W. (2004) *J. Phys. Condens. Matter*, **16**, 903.
141. Subrahmanyam, K.S., Vivekchand, S.R.C., Govindaraj, A., and Rao, C.N.R. (2008) *J. Mater. Chem.*, **18**, 1517.
142. Vivekchand, S., Rout, C., Subrahmanyam, K., Govindaraj, A.,

- and Rao, C. (2008) *J. Chem. Sci.*, **120**, 9.
143. Li, H.-Q., Wang, Y.-G., Wang, C.-X., and Xia, Y.-Y. (2008) *J. Power Source*, **185**, 1557.
 144. Stoller, M.D., Park, S., Zhu, Y., An, J., and Ruoff, R.S. (2008) *Nano Lett.*, **8**, 3498.
 145. Fan, Z., Yan, J., Zhi, L., Zhang, Q., Wei, T., Feng, J., Zhang, M., Qian, W., and Wei, F. (2010) *Adv. Mater.*, **22**, 3723.
 146. Yan, J., Wei, T., Fan, Z., Qian, W., Zhang, M., Shen, X., and Wei, F. (2010) *J. Power Source*, **195**, 3041.
 147. Yoo, E., Kim, J., Hosono, E., Zhou, H.-s., Kudo, T., and Honma, I. (2008) *Nano Lett.*, **8**, 2277.
 148. Liu, Z., Liu, Q., Huang, Y., Ma, Y., Yin, S., Zhang, X., Sun, W., and Chen, Y. (2008) *Adv. Mater.*, **20**, 3924.
 149. Blake, P., Brimicombe, P.D., Nair, R.R., Booth, T.J., Jiang, D., Schedin, F., Ponomarenko, L.A., Morozov, S.V., Gleeson, H.F., Hill, E.W., Geim, A.K., and Novoselov, K.S. (2008) *Nano Lett.*, **8**, 1704.
 150. Wang, X., Zhi, L., Tsao, N., Tomovic, Z., Li, J., and Müllen, K. (2008) *Angew. Chem. Int. Ed.*, **120**, 3032.
 151. Liu, Q., Liu, Z., Zhang, X., Yang, L., Zhang, N., Pan, G., Yin, S., Chen, Y., and Wei, J. (2009) *Adv. Funct. Mater.*, **19**, 894.
 152. Wang, F., Zhang, Y., Tian, C., Girit, C., Zettl, A., Crommie, M., and Shen, Y.R. (2008) *Science*, **320**, 206.
 153. Xia, F., Mueller, T., Lin, Y.-M., Valdes-Garcia, A., and Avouris, P. (2009) *Nat. Nanotechnol.*, **4**, 839.
 154. Ryzhii, V., Ryzhii, M., and Otsuji, T. (2008) *Appl. Phys. Exp.*, **1**, 013001.
 155. Ryzhii, V., Ryzhii, M., Ryabova, N., Mitin, V., and Otsuji, T. (2009) *Jpn. J. Appl. Phys.*, **48**, 04C144.
 156. Chitara, B., Panchakarla, L.S., Krupanidhi, S.B., and Rao, C.N.R. (2011) *Adv. Mater.*, doi: 10.1002/adma.201101414
 157. Rana, F., George, P.A., Strait, J.H., Dawlaty, J., Shivaraman, S., Chandrashekhar, M., and Spencer, M.G. (2009) *Phys. Rev. B*, **79**, 115447.
 158. George, P.A., Strait, J., Dawlaty, J., Shivaraman, S., Chandrashekhar, M., Rana, F., and Spencer, M.G. (2008) *Nano Lett.*, **8**, 4248.
 159. LeeEduardo, J.H., Balasubramanian, K., Weitz, R.T., Burghard, M., and Kern, K. (2008) *Nat. Nanotechnol.*, **3**, 486.
 160. Xia, F., Mueller, T., Golizadeh-Mojarad, R., Freitag, M., Lin, Y.-m., Tsang, J., Perebeinos, V., and Avouris, P. (2009) *Nano Lett.*, **9**, 1039.
 161. Mueller, T., Xia, F., Freitag, M., Tsang, J., and Avouris, P. (2009) *Phys. Rev. B*, **79**, 245430.
 162. Lee, C., Kim, J.Y., Bae, S., Kim, K.S., Hong, B.H., and Choi, E.J. (2011) *Appl. Phys. Lett.*, **98**, 071905.
 163. Chitara, B., Krupanidhi, S.B., and Rao, C.N.R. (2011) *Appl. Phys. Lett.*, **99**, 113114.
 164. Eda, G., Unalan, H.E., Rupesinghe, N., Amaratunga, G.A.J., and Chhowalla, M. (2008) *Appl. Phys. Lett.*, **93**, 233502.
 165. Malesevic, A., Kemps, R., Vanhulsel, A., Chowdhury, M.P., Volodin, A., and Van Haesendonck, C. (2008) *J. Appl. Phys.*, **104**, 084301.
 166. Jung, S.M., Hahn, J., Jung, H.Y., and Suh, J.S. (2006) *Nano Lett.*, **6**, 1569.
 167. Palnitkar, U.A., Kashid, R.V., More, M.A., Joag, D.S., Panchakarla, L.S., and Rao, C.N.R. (2010) *Appl. Phys. Lett.*, **97**, 063102.
 168. Prashant, K., Panchakarla, L.S., Bhat, S.V., Urmimala, M., Subrahmanyam, K.S., and Rao, C.N.R. (2010) *Nanotechnology*, **21**, 385701.
 169. Subrahmanyam, K.S., Kumar, P., Nag, A., and Rao, C.N.R. (2010) *Solid State Commun.*, **150**, 1774.
 170. Robertson, J. and O'Reilly, E.P. (1987) *Phys. Rev. B*, **35**, 2946.
 171. Bredas, J.L., Silbey, R., Boudreaux, D.S., and Chance, R.R. (1983) *J. Am. Chem. Soc.*, **105**, 6555.
 172. Seshadri, R., Rao, C.N.R., Pal, H., Mukherjee, T., and Mittal, J.P. (1993) *Chem. Phys. Lett.*, **205**, 395.
 173. Dong, X., Fu, D., Fang, W., Shi, Y., Chen, P., and Li, L.-J. (2009) *Small*, **5**, 1422.
 174. Jung, N., Kim, N., Jockusch, S., Turro, N.J., Kim, P., and Brus, L. (2009) *Nano Lett.*, **9**, 4133.

175. Ghosh, S., Chaitanya Sharma Y, S.R.K., Pati, S.K., and Rao, C.N.R. (2012) *RSC Adv.*, **2**, 1181–1188.
176. Choudhury, D., Das, B., Sarma, D.D., and Rao, C.N.R. (2010) *Chem. Phys. Lett.*, **497**, 66.
177. Saha, S.K., Chandrakanth, R.C., Krishnamurthy, H.R., and Waghmare, U.V. (2009) *Phys. Rev. B*, **80**, 6.
178. Manna, A.K. and Pati, S.K. (2010) *Nanoscale*, **2**, 1190.
179. Wildgoose, G.G., Banks, C.E., and Compton, R.G. (2006) *Small*, **2**, 182.
180. Voggu, R., Pal, S., Pati, S.K., and Rao, C.N.R. (2008) *J. Phys. Condens. Matter*, **20**, 5.
181. Kamat, P.V. (2009) *J. Phys. Chem. Lett.*, **1**, 520.
182. Muszynski, R., Seger, B., and Kamat, P.V. (2008) *J. Phys. Chem. C*, **112**, 5263.
183. Subrahmanyam, K.S., Manna, A.K., Pati, S.K., and Rao, C.N.R. (2010) *Chem. Phys. Lett.*, **497**, 70.
184. Si, Y. and Samulski, E.T. (2008) *Chem. Mater.*, **20**, 6792.
185. Li, Y., Fan, X., Qi, J., Ji, J., Wang, S., Zhang, G., and Zhang, F. (2010) *Nano Res.*, **3**, 429.
186. Guo, S., Dong, S., and Wang, E. (2009) *ACS Nano*, **4**, 547.
187. Hong, W., Bai, H., Xu, Y., Yao, Z., Gu, Z., and Shi, G. (2010) *J. Phys. Chem. C*, **114**, 1822.
188. Wang, Y., Ni, Z., Hu, H., Hao, Y., Wong, C.P., Yu, T., Thong, J.T.L., and Shen, Z.X. (2010) *Appl. Phys. Lett.*, **97**, 163111.
189. Ma, J., Zhang, J., Xiong, Z., Yong, Y., and Zhao, X.S. (2010) *J. Mater. Chem.*, **21**, 3350.
190. Xu, C., Wang, X., and Zhu, J. (2008) *J. Phys. Chem. C*, **112**, 19841.
191. Williams, G. and Kamat, P.V. (2009) *Langmuir*, **25**, 13869.
192. Das, B., Choudhury, B., Gomathi, A., Manna, A.K., Pati, S.K., and Rao, C.N.R. (2011) *Chem. Phys. Chem.*, **12**, 937.
193. Patchkovskii, S., Tse, J.S., Yurchenko, S.N., Zhechkov, L., Heine, T., and Seifert, G. (2005) *Proc. Natl. Acad. Sci. U.S.A.*, **102**, 10439.
194. Ghosh, A., Subrahmanyam, K.S., Krishna, K.S., Datta, S., Govindaraj, A., Pati, S.K., and Rao, C.N.R. (2008) *J. Phys. Chem. C*, **112**, 15704.
195. Kumar, N., Subrahmanyam, K.S., Chaturbedy, P., Raidongia, K., Govindaraj, A., Hembram, K.P.S.S., Mishra, A.K., Waghmare, U.V., and Rao, C.N.R. (2011) *Chem. Sus. Chem.*, **4**, 1662–1670.
196. Stankovich, S., Dikin, D.A., Dommett, G.H.B., Kohlhaas, K.M., Zimney, E.J., Stach, E.A., Piner, R.D., Nguyen, S.T., and Ruoff, R.S. (2006) *Nature*, **442**, 282.
197. Ramanathan, T., Abdala, A.A., Stankovich, S., Dikin, D.A., Herrera-Alonso, M., Piner, R.D., Adamson, D.H., Schniepp, H.C., Chen, X., Ruoff, R.S., Nguyen, S.T., Aksay, I.A., Prud'Homme, R.K., and Brinson, L.C. (2008) *Nat. Nanotechnol.*, **3**, 327.
198. Das, B., Prasad, K.E., Ramamurty, U., and Rao, C.N.R. (2009) *Nanotechnology*, **20**, 125705.
199. Rafiee, M.A., Rafiee, J., Wang, Z., Song, H., Yu, Z.-Z., and Koratkar, N. (2009) *ACS Nano*, **3**, 3884.
200. Prasad, K.E., Das, B., Maitra, U., Ramamurty, U., and Rao, C.N.R. (2009) *Proc. Natl. Acad. Sci. U.S.A.*, **106**, 13186.
201. Voggu, R., Das, B., Rout, C.S., and Rao, C.N.R. (2008) *J. Phys. Condens. Matter*, **20**, 472204.
202. Subrahmanyam, K.S., Voggu, R., Govindaraj, A., and Rao, C.N.R. (2009) *Chem. Phys. Lett.*, **472**, 96.
203. Varghese, N., Ghosh, A., Voggu, R., Ghosh, S., and Rao, C.N.R. (2009) *J. Phys. Chem. C*, **113**, 16855.
204. Lu, C.-H., Yang, H.-H., Zhu, C.-L., Chen, X., and Chen, G.-N. (2009) *Angew. Chem. Int. Ed.*, **48**, 4785.
205. Kim, J., Cote, L.J., Kim, F., and Huang, J. (2009) *J. Am. Chem. Soc.*, **132**, 260.
206. Xie, L., Ling, X., Fang, Y., Zhang, J., and Liu, Z. (2009) *J. Am. Chem. Soc.*, **131**, 9890.
207. Xu, Y., Liu, Z., Zhang, X., Wang, Y., Tian, J., Huang, Y., Ma, Y., Zhang, X., and Chen, Y. (2009) *Adv. Mater.*, **21**, 1275.

208. Xu, Y., Zhao, L., Bai, H., Hong, W., Li, C., and Shi, G. (2009) *J. Am. Chem. Soc.*, **131**, 13490.
209. Ramakrishna Matte, H.S.S., Subrahmanyam, K.S., Venkata Rao, K., George, S.J., and Rao, C.N.R. (2011) *Chem. Phys. Lett.*, **506**, 260.
210. Álvaro, M., Atienzar, P., Bourdelande, J.L., and García, H. (2004) *Chem. Phys. Lett.*, **384**, 119.
211. Shafirovich, V.Y., Levin, P.P., Kuzmin, V.A., Thorgeirsson, T.E., Kliger, D.S., and Geacintov, N.E. (1994) *J. Am. Chem. Soc.*, **116**, 63.
212. Elias, D.C., Nair, R.R., Mohiuddin, T.M.G., Morozov, S.V., Blake, P., Halsall, M.P., Ferrari, A.C., Boukhvalov, D.W., Katsnelson, M.I., Geim, A.K., and Novoselov, K.S. (2009) *Science*, **323**, 610.
213. Jaiswal, M., Yi Xuan Lim, C.H., Bao, Q., Toh, C.T., Loh, K.P., and Ozyilmaz, B. (2011) *ACS Nano*, **5**, 888.
214. Xie, L., Jiao, L., and Dai, H. (2010) *J. Am. Chem. Soc.*, **132**, 14751.
215. Jones, J.D., Hoffmann, W.D., Jesseph, A.V., Morris, C.J., Verbeck, G.F., and Perez, J.M. (2010) *Appl. Phys. Lett.*, **97**, 233104.
216. Zheng, L., Li, Z., Bourdo, S., Watanabe, F., Ryerson, C.C., and Biris, A.S. (2010) *Chem. Commun.*, **47**, 1213.
217. Gopalakrishnan, K., Subrahmanyam, K.S., Kumar, P., Govindaraj, A., and Rao, C.N.R., (2012) *RSC Adv.*, **2**, 1605–1608.
218. Ramakrishna Matte, H.S.S., Gomathi, A., Manna, A.K., Late, D.J., Datta, R., Pati, S.K., and Rao, C.N.R. (2010) *Angew. Chem. Int. Ed.*, **49**, 4059.
219. Yang, D., Sandoval, S.J., Divigalpitiya, W.M.R., Irwin, J.C., and Frindt, R.F. (1991) *Phys. Rev. B*, **43**, 12053.
220. Gordon, R.A., Yang, D., Crozier, E.D., Jiang, D.T., and Frindt, R.F. (2002) *Phys. Rev. B*, **65**, 125407.
221. Schumacher, A., Scandella, L., Kruse, N., and Prins, R. (1993) *Surf. Sci.*, **289**, L595.
222. Yang, D. and Frindt, R.F. (1999) *J. Phys. Chem. Solids*, **57**, 1113.
223. Matte, H.S.S.R., Plowman, B., Datta, R., and Rao, C.N.R. (2011) *Dalton Trans.*, **40**, 10322.
224. Nag, A., Raidongia, K., Hembram, K.P.S.S., Datta, R., Waghmare, U.V., and Rao, C.N.R. (2010) *ACS Nano*, **4**, 1539.
225. Kumar, N., Raidongia, K., Mishra, A.K., Waghmare, U.V., Sundaresan, A., and Rao, C.N.R. (2011) *J Solid State Chem.*, **184**, 2902.
226. Raidongia, K., Nag, A., Hembram, K.P.S.S., Waghmare, U.V., Datta, R., and Rao, C.N.R. (2010) *Chem. Eur. J.*, **16**, 149.
227. Radisavljevic, B., Radenovic, A., Brivio, J., Giacometti, V., and Kis, A. (2011) *Nat. Nanotechnol.*, **6**, 147.
228. Kiran, M.S.R.N., Raidongia, K., Ramamurthy, U., and Rao, C.N.R. (2011) *Scr. Mater.*, **64**, 592.

